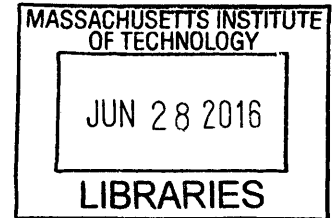# Structure and Performance of Carbon Xerogel Molded Emitters for Micropropulsion Applications

by

Iulia Elena Jivanescu

B.S. Aerospace Engineering
Polytechnic University of Bucharest, 2012

Submitted to the Department of Aeronautics and Astronautics
In partial fulfillment of the requirements for the degree of

Master of Science in Aeronautics and Astronautics

at the

MASSACHUSETTS INSTITUTE OF TECHNOLOGY

June 2016

Author.. **Signature redacted**

Department of Aeronautics and Astronautics
May 19, 2016

Certified by.. **Signature redacted**

Paulo C. Lozano
Associate Professor of Aeronautics and Astronautics
Thesis Supervisor

Accepted by... **Signature redacted**

Paulo C. Lozano
Associate Professor of Aeronautics and Astronautics
Chair, Graduate Program Committee

Structure and Performance of Carbon Xerogel Molded Emitters for Micropropulsion Applications

by

Iulia Elena Jivanescu

Abstract

Ion electrospray propulsion relies on the transport of propellant to emission sites where ions and/or droplets are extracted to create thrust. The focus of this research is the creation of porous emitter substrates through which the liquid is passively transported. Previous substrates were created subtractively by selectively removing material to reveal emitter tips or arrays. The limitations of the previous substrates are pore size variability, non-uniform emitter tips, and difficulty in creating identical tips. This study investigates the use of carbon xerogels for electrospray applications due to their exceptional properties such as large surface to volume ratio, robustness and pore uniformity. The substrates are created through a synthesis route which is advantageous for reproducibility. Single carbon xerogel emitter tips and emitter arrays are molded on previously synthesized carbon xerogel substrates. Molding is an additive method which allows for parallel processing and batch manufacturing. Initially carbon xerogels substrates are synthesized. Then a carbon xerogel emitter tip is molded on top of a previously synthesized carbon substrate. Finally, an array of resorcinol formaldehyde emitters is molded on top of a carbon substrate. The carbon xerogel substrate with a molded tip is tested for Retarding Potential Analysis and Time of Flight Mass Spectrometry measurements in order to determine fragmentation fractions and beam composition. The results are consistent with the ionic liquid EMI-BF$_4$ fragmentation fractions and pure ionic regime is achieved. The beam is nearly monoenergetic and fragmentation occurs mostly outside the acceleration region which does not affect thruster efficiency.

Thesis Supervisor: Paulo C. Lozano
Title: Associate Professor of Aeronautics and Astronautics

Acknowledgements

I would like to thank my advisor, Prof. Paulo Lozano, for making my dream of learning and working in space propulsion come true. I am thankful for his continuous support, guidance and expertise and for giving me the opportunity to be part of the Space Propulsion Lab.

I would like to thank my friend and colleague Catherine for sharing her knowledge and experience, for helping me with my experiments and for answering all my questions. I would like to thank my friend Ioana who was a true support over the last year.

Everyone at SPL is worthy of my deepest thanks. I would like to thank Corey, Carla, Carmen, Kento, David, Fernando, Alex, Chase, Dakota, Ewan, Jeff and Nancy. You all played a part in my development at MIT. I would like to thank the UROPs Tori, Alejandro and Jason for their help along the way. I would like to thank Jimmy for making lab work a lot of fun and Todd for his help in the machine shop.

I would like to thank my mother who always told me to be courageous and my father for inspiring me with the love for aerospace engineering. I would like to thank my grandparents Mica, Toto, Didi and A, who took close care of me and who helped me develop into the person that I am today. I would like to thank my family in the US who made my time here very enjoyable. I would like to thank Cristina for her support and wise advice. Hello to my baby sister Luana, who always makes me smile. Soon you will be able to pronounce my name.

Thank you to all my old friends. I cannot wait to spend more time with all of you. Thank you to all my new friends that I made at MIT. I have learned so much from you and I hope to see you again soon.

Finally, I would like to thank Stéphane for his continuous support, inspiration and encouragement and for making life beautiful.

Table of Contents

List of Figures

9

10

List of Tables

Chapter 1

Introduction

The miniaturization of electronics has enabled the construction of very small satellites known as CubeSats. From the family of CubeSats, the nanosatellites (1-10 kg) and the microsatellites (10-100 kg) have received most attention from academia and industry. However, only a few of them have an onboard propulsion system. A propulsion system enables change of orbit, counteracts atmospheric drag and allows escape from Earth's orbit, greatly enhancing the capabilities of the mission. Therefore, the more recent spacecraft mission designs often dictate the need for an onboard propulsion system. This can be used for attitude control, main propulsion or both.

Despite rapid developments in miniaturized electronics, there is still a gap in the development of micropropulsion systems. The most simple propulsion system available is the cold gas which works by releasing high pressure gas to produce thrust. This is very limited as it produces low thrust and low specific impulse. Existing electric propulsion systems (e.g. plasma thrusters – ion engines and Hall Thrusters) can be employed only on larger missions. Ion engines are better suited for very long missions such as deep space exploration while Hall thrusters provide higher thrust to power ratios in missions like orbital corrections. Both of these technologies have power levels ranging from 200 W to 10's of kW, leaving both ends of very low and very high power levels uncovered. Very low power levels are beneficial for micropropulsion as very small forces are required. Larger missions, such as human exploration of the solar system, demand very high power electric propulsion which could be achieved by coupling with low mass-to-power electric generators and nuclear reactors. This is where the miniaturized electric propulsion finds its niche by offering high specific impulse and ability to operate at very low and possibly very high power levels.

Miniaturized electric propulsion has numerous potential applications. It can be employed on CubeSats for scientific missions such as astrophysics – search of exoplanets, interplanetary exploration, weather monitoring, remote sensing and biological research. It can be used for satellite servicing and station keeping, formation flying for interferometry or gravitational wave detection and for precision pointing for communications.

1.1 Space Propulsion metrics

To better understand the difference between chemical and electric propulsion we introduce the notions of specific impulse and thrust. Chemical propulsion systems offer much higher thrust for a short period of time and a lower specific impulse, while electric propulsion offers higher specific impulse and lower thrust for longer periods of time.

The thrust F from a space propulsion system is given by the equation below. Here $\dot{m}$ represents the propellant mass flow rate used for propulsion and c is the exhaust velocity.

$$F = \dot{m}c$$

Specific impulse reveals how effectively the propulsion system delivers the impulse to fulfill the mission requirements, by representing the ability of a propulsion system to use a unit of mass of propellant. The specific impulse equals the impulse per unit weight of propellant.

$$I_{sp} = \frac{\int_0^t F\,dt'}{W_p} = \frac{\int_0^t \dot{m}c\,dt'}{g \int_0^t \dot{m}\,dt'}$$

For constant exhaust velocity, the specific impulse will become

$$I_{sp} = \frac{c}{g} = \frac{F}{\dot{m}g}$$

where g is the gravitational acceleration of Earth (9.81 m/s^2).

In chemical rockets the chemical energy is transformed into thermal energy by means of expanding gas through a nozzle and the specific impulse has maximum values of ~ 450 s. Electric propulsion engines can achieve a much higher specific impulse, up to thousands of seconds. An example would be the Dawn mission, propelled by three ion engines that have a specific impulse of 3100 s and a thrust of 90 mN. In chemical rockets the propulsive power is given by the energy stored in the chemical bonds of the propellant while in electrical rockets the propulsive power is given by an electric power source.

The efficiency of the propulsion system defines its ability to convert input electric power P (the product of net input current I and voltage V) into useful thrust power and is given by

16

$$\eta = \frac{\frac{1}{2}\dot{m}c^2}{P}$$

The rocket equation, which is obtained by integrating Newton's second law for a propulsive maneuver and for constant specific impulse is given by

$$m_p = m_0 \left(1 - e^{\frac{-\Delta V}{g\, I_{sp}}} \right)$$

where m_p represents the mass of propellant and m_0 the initial spacecraft mass.

This equation reveals that a propulsive mission can be described in terms of its ΔV, which represents the change in velocity in a force free environment. For a higher specific impulse, a lower propellant mass is required for missions performing the same ΔV. However, since thrust is dependent on power, specific impulse and efficiency, for a mission with fixed power budget and efficiency, a very high specific impulse would result in the decrease of thrust:

$$F = \frac{2\, P\, \eta}{g\, I_{sp}}$$

1.2 Space Propulsion state of the art

Depending on the source of energy the thrusters can be categorized into chemical and electrical. The chemical rockets can be divided into cold gas, monopropellant, bipropellant and solid propellant. Out of these only the cold gas does not use the chemical energy stored in the chemical bonds to produce thrust. It functions by accelerating an inert pressurized gas through a nozzle and it has very limited delta V and thrust capabilities. Monopropellant thrusters rely on the decomposition of only one fuel with the aid of a catalyst and provide a high temperature gas which is accelerated through a nozzle. Typical propellants are Hydrazine and Hydrogen Peroxide. They produce a specific impulse in the range of 150-220 s and a thrust up to 500 N. Bipropellants rely on combining a fuel with an oxidizer to release the energy stored in the bonds. They produce higher specific impulse and thrust values but they are more complex as they require a

pressurization system – gas or turbomachinery pressurized. The SSME used LOX and LH2 as propellants and achieved a specific impulse of 450 s and 2279 kN of thrust in vacuum. Solid propellant engines work by combining solid fuel and solid oxidizer along with other additives. They can provide a specific impulse up to 300 s and MN levels of thrust. The disadvantage of this propulsion system is that once started it cannot be stopped, and it burns until the depletion of propellant [1].

Electrical propulsion systems can be divided into augmented, electrostatic, electromagnetic and radio-frequency thrusters. The augmented thrusters are chemical thrusters in which electrical energy is added in order to increase the thermal energy of the gas prior to expansion. This increases the specific impulse which can reach values of 1000 s for arcjets thrusters with H_2. The thrusters can be divided into resistojets and arcjets. The most common electric propulsion systems are the ion engines (electrostatic) and the Hall thrusters (electromagnetic). They work by accelerating charged particles through an electric potential. Ion engines and Hall thrusters work by ionizing a noble gas (typically argon or xenon) and then accelerating it. The ionization is different for the two systems. Ion engines use electron bombardment or radio frequency (RF), where electrons are emitted from a cathode and confined by a magnetic field that increases their residence time in the dedicated ionization region. Some of the ions created migrate to the acceleration region through a set of grids and fall through a potential drop which produces thrust. The specific impulse achieved by these engines can go up to 4000 s while the thrust density (thrust per unit area) levels rise up to a few Newtons per square meter. The ionization in Hall thrusters is slightly different, the injected gas being ionized by electrons that execute an annular $\vec{E} \times \vec{B}$ drift. The ions are accelerated through an electric potential between the anode at the beginning of the annular chamber and an external cathode. They have a specific impulse ranging from 1500 s to 2500 s and thrust density levels ten times higher than ion engines. In electrostatic devices the electrostatic forces that accelerate the ions are felt directly by an electrode and this is how thrust is created. Hall thrusters are pushed magnetically as electrons are stopped axially by the magnetic field, and subsequently exerting the same force on the magnetic assembly. Thrusters that use magnetic forces only can supply thrust densities up to 8000 N/m^2, have lower efficiencies and can operate for short period of times. Examples include the magneto plasma dynamic (MPD) thrusters, the applied field MPD thrusters, the Pulsed Plasma Thrusters (PPT), the Pulsed Inductive Thrusters (PIT) [1].

1.3 Electrospray propulsion

The ion electrospray propulsion systems rely on the transport of propellant through a porous medium to emission regions where ions are extracted at high velocities. The propellant is an ionic liquid, a room temperature molten salt composed of both positive and negative ions. Unlike ion engines and Hall thrusters, the electrosprays do not need to ionize particles or to use a neutralizing cathode for the beam. Electrospray thrusters can avoid spacecraft charging by operating in both polarities. Two thrusters can operate next to each other, one emitting positive ions and the other emitting negative ions. This translates into power, mass and volume savings compared to plasma thrusters that require ionization and a neutralizing cathode. Another advantage over plasma thrusters is that electrospray thrusters use nearly all the propellant. In plasma thrusters a good amount of the gas is not ionized and leaks out the exit resulting in a reduced specific impulse.

Ionic liquids have zero vapor pressure due to strong Coulomb forces between ions. Therefore, they do not evaporate in vacuum and do not require a pressurization system. They are passively fed through the porous medium to the tips through capillary forces alone. This removes the need for a propellant feed system. The emission is referred to as an ionic liquid ion source (ILIS) when pure ions are emitted. The thrust per emitter is very small (10 nN) and therefore clustering is necessary to achieve the desired thrust. The clustering of these tips gives rise to an emitter array. Figure 1-1 is a scanning electron microscope (SEM) picture of such an array [2].
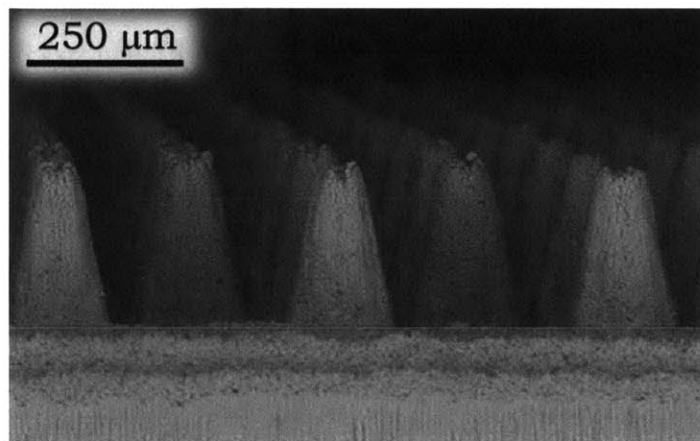
Figure 1-1 – SEM picture of an ion electrospray emitter array [2]

The ion extraction is achieved by applying a difference of potential between the conductive ionic liquid and an extractor grid. The conductive liquid that is fed to the tips rises up as it is perturbed by the electric field to form a structure called a Taylor cone. Liquid evolves into a Taylor cone when the electrostatic pressure and surface tension are balanced. If stressed enough the emission of droplets or ions could occur from the surface of the liquid. As the system has a passively fed mechanism for liquid transport, a micro-rocket is created. A diagram of the Taylor cone formation and emission can be seen in Figure 1-2. At the emission site the Taylor cone solution is no longer valid as charges are removed.
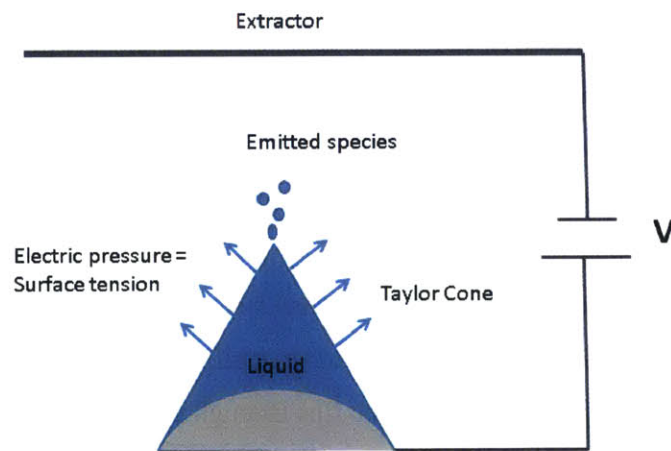
Figure 1-2 – Taylor Cone formation

The emission can be composed of ions, droplets or a mixture of both. The highest efficiency (100 %) can be achieved with either pure ionic regime or pure droplet regime. The combination of these two lowers the efficiency. The two distinct modes give different specific impulse. The ionic mode has a higher specific impulse, up to 3500 s, depending on the ionic liquid, while the droplet regime has values of up to 300 s. This can be seen by approximating the beam velocity by

$$c_i = \sqrt{\frac{2\,q_i V}{m_i}}$$

where q_i/m_i is the charge to mass ratio and V is the extracting potential. Ions are species with higher charge to mass ratios than droplets and therefore the exhaust velocity and specific impulse have higher values. The applied voltage can range between 1 and 2 kV. The droplet regime has

higher flow rates than the ionic regime, which translates into higher thrust density. In this research we are interested in the ionic regime, as it operates with low flow rates that enable the use of a passively fed liquid transport.

Electrospray emitters can be divided into capillaries, externally wetted and internally wetted emitters. The capillary emitters use pressure or capillarity to provide liquid to the tip. They usually operate in the droplet mode, with higher thrust, higher flow rates and lower efficiency. Externally wetted emitters rely on surface wetting to provide the transport of propellant. This configuration allows for the miniaturization of the propulsion system and can achieve pure ionic regime (PIR). The internally wetted emitters or the porous emitters came as a response to the need of increasing the amount of current that was carried towards the emission regions while allowing for microfabrication techniques. The different categories of emitters can be seen in Figure 1-3.
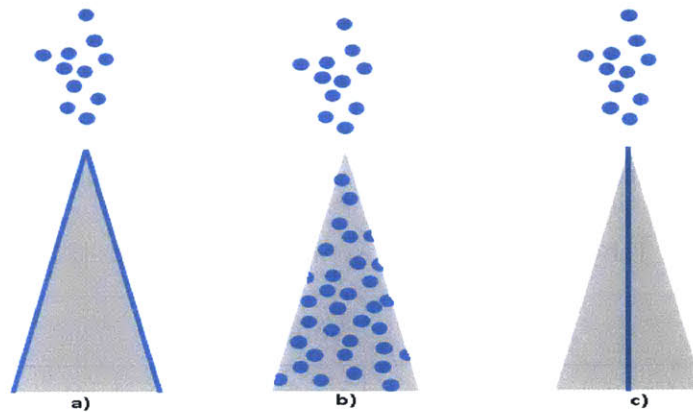
Figure 1-3 – Types of emitters. The grey area represents the emitter itself, pointing upwards, and the blue represents propellant. Shown from left to right are: a) externally wetted; b) porous emitter; c) capillary emitter

1.4 Electrospray propulsion state of the art

Courtney introduced the first ion electrospray thruster concept composed of propellant tank, emitter substrate and extractor electrode. He created the first nickel emitter arrays on silicon

frames [3]. The state of the art thruster has a laser ablated porous borosilicate emitter substrate. The tips are 300 μm tall, 20 μm wide and are spaced on a 450 μm hexagonal lattice. The limitations of the porous borosilicate glass are non-uniform pore sizes which translate into non-uniform emitters and wetting issues of the arrays. The porous glass is commercially acquired and subsequently laser ablated. The state of the art thruster can be seen in Figure 1-4 and the measured performance metrics are given in Table 1-1.
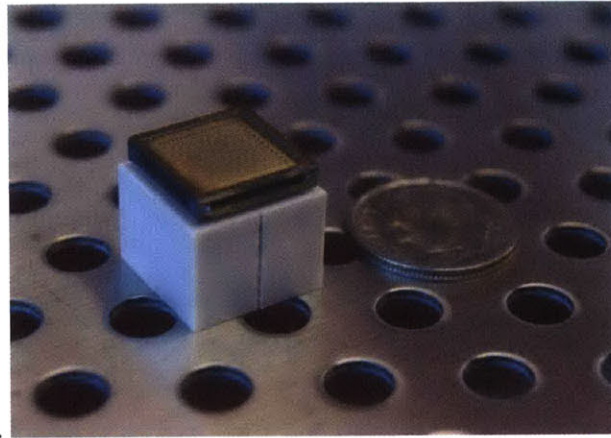
Figure 1-4 – State of the art ion electrospray thruster [4]

Table 1-1 – Ion electrospray thruster metrics [21]

Metric	Value
Engine Mass	3.5 g
Engine Dimensions	14.4 mm x 14.4 mm x 14.1 mm
Specific Impulse	1150 s
Thrust	12.5 μN
Nominal Power	0.138 W

1.5 Contributions

This research focuses on manufacturing techniques of ion electrospray emitter substrates. It investigates the use of carbon xerogels for electrospray applications due to their large surface-area-to-volume and exceptional pore size uniformity. The synthesis route of carbon xerogels is much more advantageous for reproducibility than previously acquired porous substrates. The synthesis route improves emitter shape control and pore structure uniformity and should enhance the performance and lifetime of thrusters. Previous substrates were shaped into emitter arrays by subtractive methods, in which material was removed to reveal the desired structures. This research focuses on additive methods, in which both carbon xerogel single emitter tips and carbon xerogel arrays are molded on a carbon substrate using the same synthesis route. For the molded single emitter tip current versus voltage curves, retarding potential analysis (RPA) and time of flight mass spectrometry (TOF) measurements are presented. The goal of this method is towards serial batching and parallel processing, while having a porous substrate and a high density of tips that can either be externally or internally wetted.

Chapter 2

Review of Methods of Fabrication

The role of the emitter substrate is to transport liquid to the emission sites. The fabrication of arrays for micro-propulsion started with arrays on silicon. As transport of liquid was an issue the focus shifted towards porous materials, at first porous metals and then porous glass and alumina xerogels. The state of the art is given by porous borosilicate glass.

2.1 Silicon arrays

Work on silicon arrays was performed by Garza, Velasquez-Garcia, Gassend, Krpoun and Shea. Krpoun and Shea focused on providing propellant transport in an active way with the use of a pressurized feed system. They developed thrusters by clustering silicon capilaries filled with ceramic microbeads. The emission was both droplet and purely ionic and they used ionic liquid as propellant [5]. A picture of a capillary emitter can be seen in figure 2-1 a). Externally wetted silicon arrays were researched by Garza, Velasquez-Garcia and Gassend [6 7, 8, 9, 10]. The difference from the porous feeding of propellant is that they rely on surface transport of liquid to the emission sites. Black silicon was investigated as a means of roughening the surface of the silicon in order to enhance the transport of propellant by increasing the wettability of the material. Roughening the surface of the silicon can be achieved in at least three ways: laser etching, gold etching or plasma etching. Thrusters were assembled via microelectromechanical systems (MEMS) and the fabrication was achieved by Deep Reactive Ion Etching (DRIE) and wafer bonding [6]. The black silicon surface treatment is depicted in Figure 2-1 b).

Velasquez created a planar array of 1024 emitters on a 0.64 cm^2 area through plasma etching. Emission was achieved with similar levels observed in single externally wetted silicon emitters (100's nA). However, the thruster did not have an extractor grid and testing was performed by ablative emission tests [7, 8]. Gassend fabricated a planar array of 502 emitters and incorporated an extractor grid. Pure ionic emission from EMI-BF$_4$ and EMI-IM was obtained with an emission of up to 1 μA per emitter [9, 10]. Both models were limited in transporting

liquid to the emission sites. In order to achieve a constant and stable operation Velasquez suggested a pressure fed design while Gassend suggested porous materials for a passively fed design. A single emitter and an array of silicon emitters are presented in Figure 2-1 c) and d).
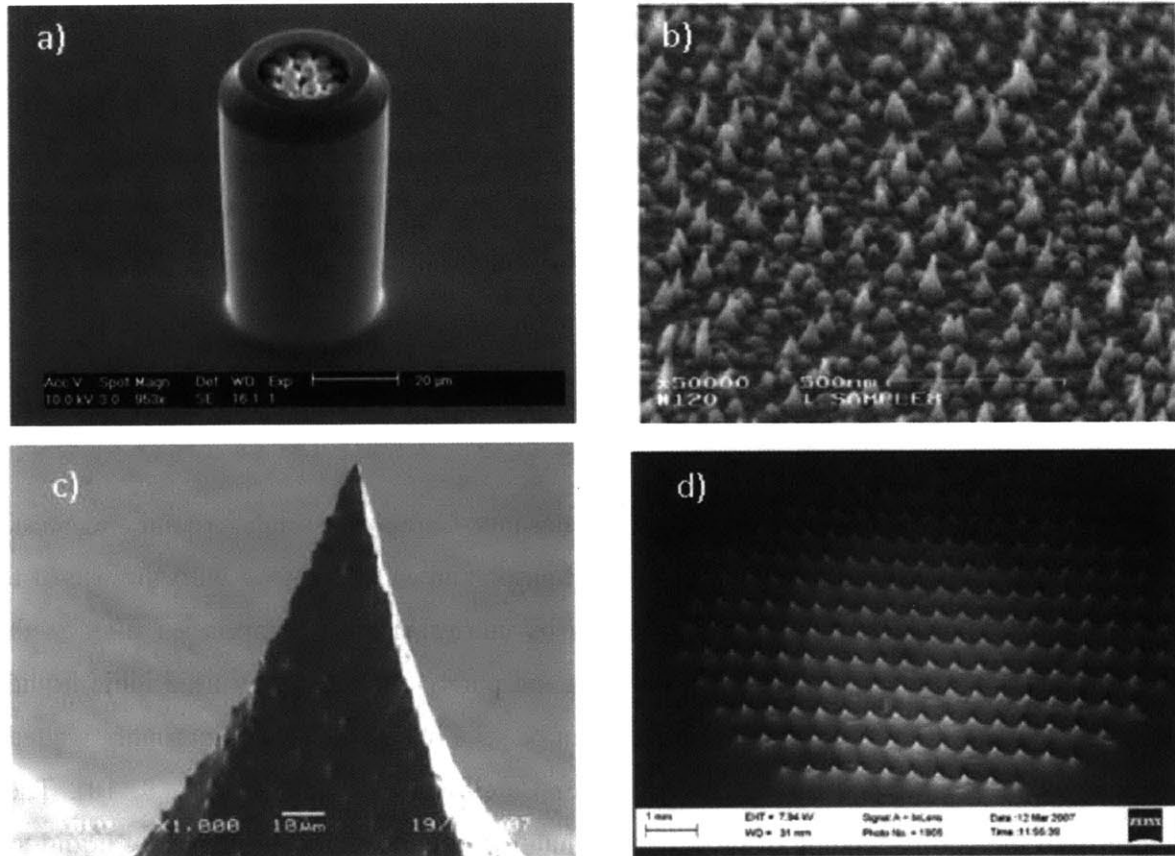
Figure 2-1 – Silicon emitters: a) silicon capillaries filled with microceramic beads [5]; b) black silicon surface treatment [6]; c) silicon single emitter [10]; d) externally wetted array of silicon emitters [10]

2.2 Porous Tungsten

In order to address the issues of liquid transport to the emission sites and stable operation Legge [11, 12, 13] investigated the use of porous tungsten. He was the first to demonstrate that porous substrates can achieve a pure ionic regime [11]. Currents of 100's of nA up to 10 μA have been observed per tip at startup voltage of 1500 V, with tip radii measuring 10-30 μm. Thrust levels of

up to 1 μN per emitter and specific impulse of ~3000 s were measured for a 49 emitter 1D array. The pore size of tungsten was ~0.5-2 μm and the porosity 30 %. Tungsten was acquired comercially. Figure 2-2 shows the microstructure of porous tungsten.
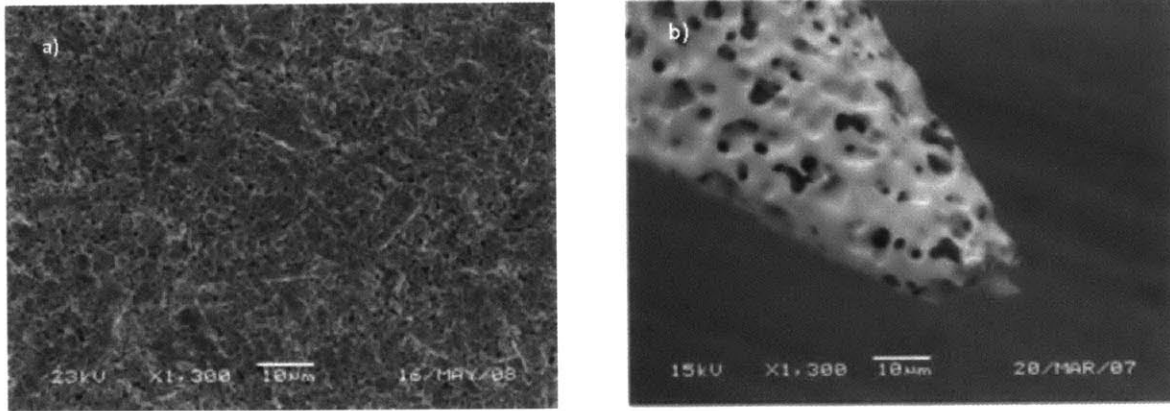
Figure 2-2 – a) 0.5 μm porous Tungsten b) Tungsten emitter tip [12]

The method of fabrication was electrochemical etching and the tungsten was patterned with a polymide masking technique. The process is shown in Figure 2-3. This selection came from the success of Lozano on electrochemically etching tungsten needles [14]. The samples were immersed in a 1N sodium hydroxide solution with an applied voltage of 6 V for 45 minutes. First the pores of the substrate were infiltrated with polymide and the substrate was masked with positive photoresist. The substrate was etched in NaOH to reveal the tips and the excess polymide in the pores was removed in a pirranha solution.
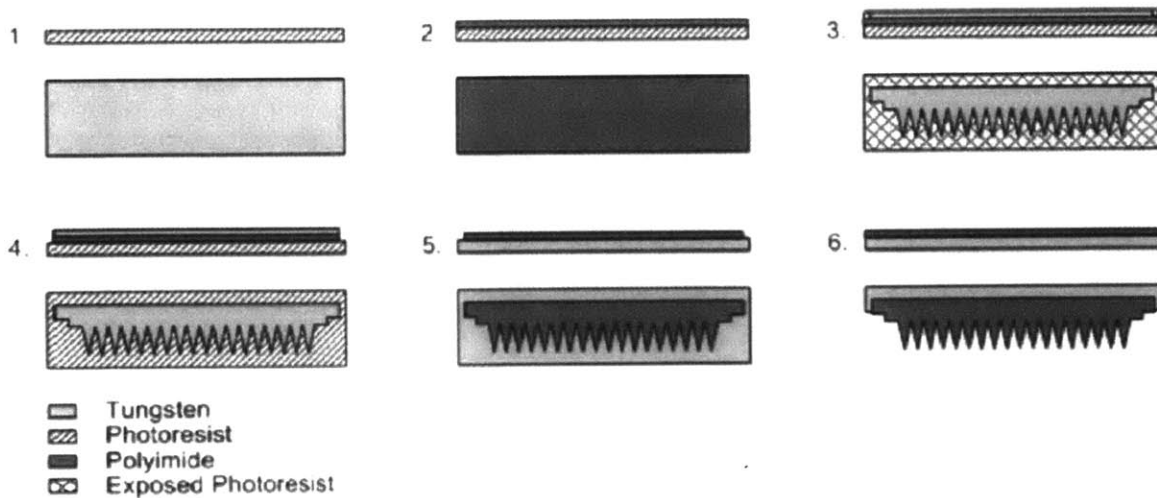
Figure 2-3 – Electrochemical etching of porous Tungsten [11]

27

Legge noted that masking issues given by the contamination of photoresist and polymide penetrating into the porous layer would be detrimental. Moreover, uniformity was limited when densification was attempted. Non uniformities became significant as the emitter spacing approached 500 μm. Various 1-D arrays are shown in Figure 2-4.
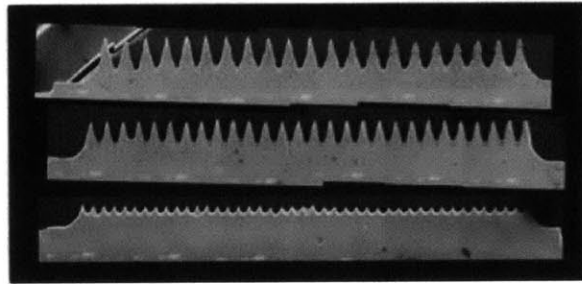
Figure 2-4 – 1-D arrays of porous Tungsten with varying emitter separation [12]

2.3 Porous Nickel

Continuing the work of Legge, Courtney used the same fabrication method of electrochemical etching and applied it to porous nickel. The etching regime employed smoothly removed material from the surface of the porous substrate without damaging the internal pore structure. Courtney developed a two step process for forming arrays using numerical simulations of the etching process in order to investigate the impact of non uniform emitters. An array of emitters obtained through this process can be seen in Figure 2-5. The porous nickel had pore sizes up to 5 μm and 45 % porosity.
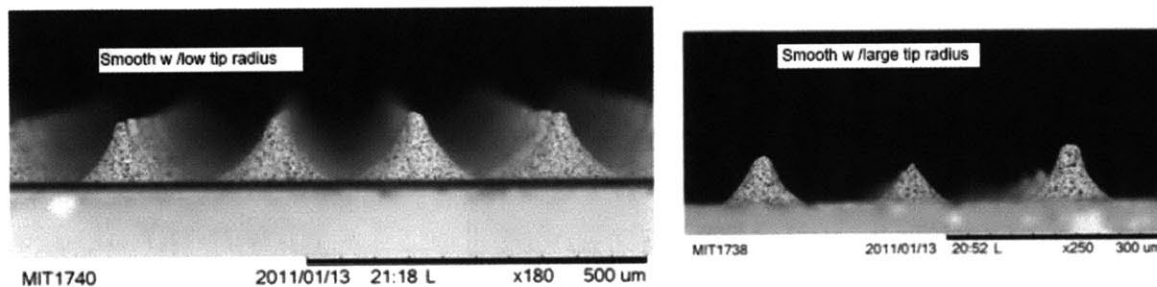
Figure 2-5 – Smooth porous Nickel emitters obtained through the secondary etch step [3]

An etching station produced arrays of 480 emitters with heights of 165 μm, spaced 500 μm apart on a 1 cm^2 nickel substrate. The substrate was first aligned with a silicon substrate package. Then the arrays were mounted and aligned with electrostatic grids and the propellant was fed to the emission sites by capillarity. The start-up voltage was 850 V and the beam current exceeded several 100's μA for both polarities. Courtney estimated that the engines could supply 10's of μN of thrust at 1500 V and a specific impulse of 2000-3000 s. The thrusters measured 1.2 x 1.2 x 0.2 cm, weighed less than 1 g and required less than 0.65 W of power [3]. The electrochemical etching process and thruster packaging is shown in Figure 2-6.
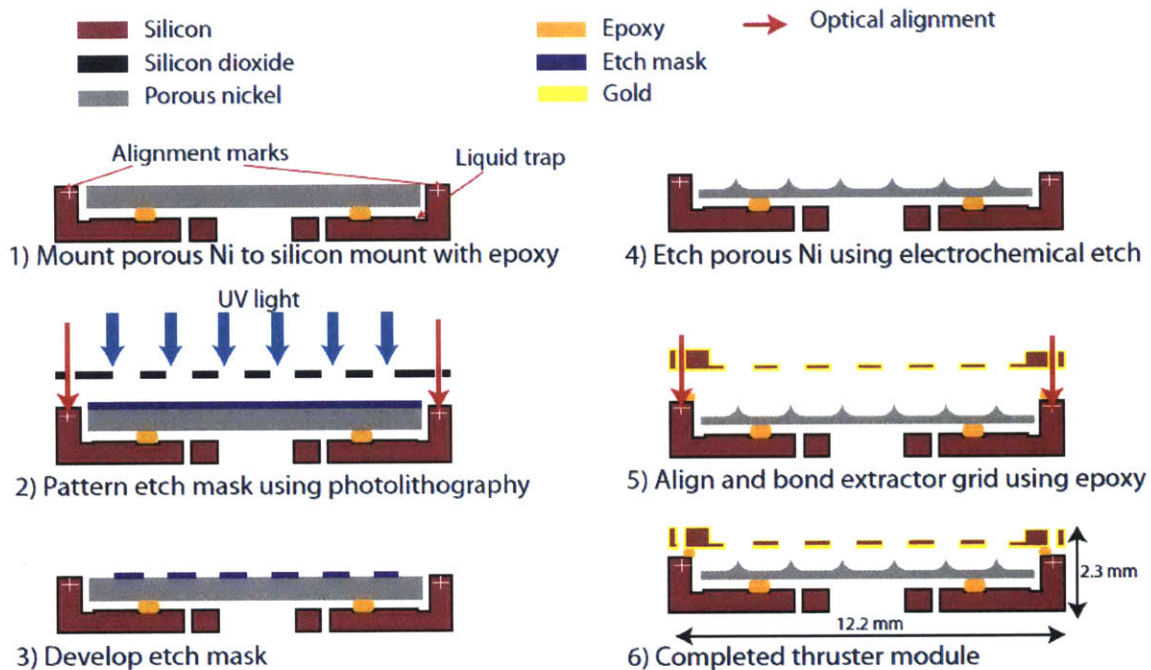
Figure 2-6 – Fabrication process for aligned arrays of porous Nickel [3]

The limitations of the etching process developed by Courtney are given by non-uniform emitter tips, which results in performance variations, and by tip degradation due to electrochemistry.

2.4 The distal electrode

Brikner and Lozano discovered that tip degradation occured because of electrochemistry during ion emission. Electrochemistry refers to chemical reactions between the source emitter and the ionic liquid. As ions of one polarity are extracted at the tip of the emission sites, ions of opposite

polarity remain behind and form an electrochemical double layer at the interface between the liquid and the electrode. Eventually, the potential layer across the double layer will reach the electrochemical window of the liquid and this results in decomposition and corrosion of the emitters. Voltage alternations can increase the lifetime of conductive porous emitters [15]. The effects of electrochemistry are geometry changes of the tips and decreased electric fields. Electrochemistry can also affect the properties of the ionic liquid [16, 17]. A picture of emitter degradation can be seen in Figure 2-7.
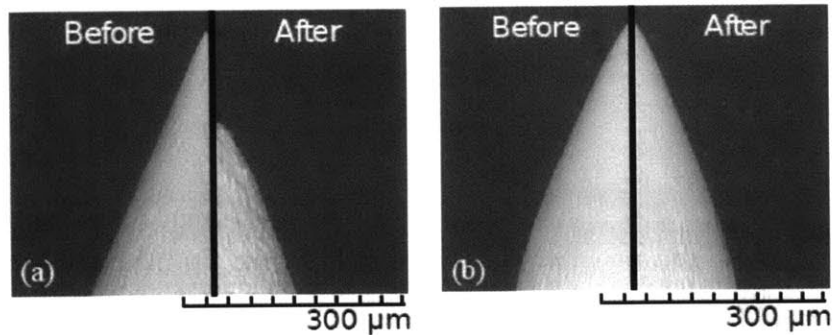
Figure 2-7 – Tungsten emitters before and after firing: a) tip etching and surface roughening; b) tip is undamaged with the implementation of the distal electrode [16]

Brikner and Lozano introduced a distal electrode upstream the emitter substrate in order to divert reactions from the emitter substrate. The distal electrode is a conductive porous material and can be implemented with both conductive and dielectric emitter substrates. The potential of the emitter varies with the potential of the ionic liquid thus preventing electrochemistry from happening at the tips. The modified schematic architecture is shown in Figure 2-8.
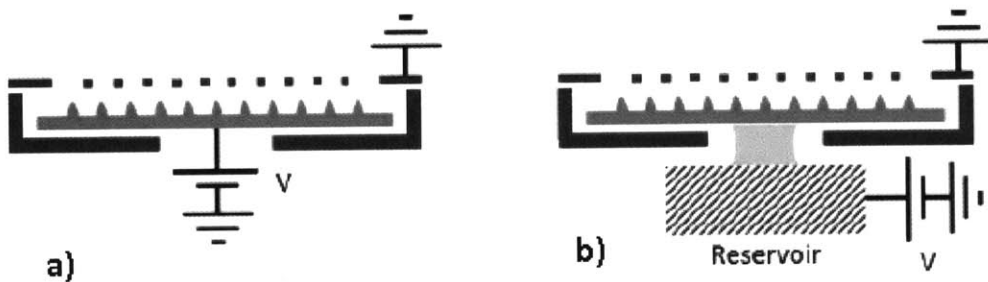
Figure 2-8 – Electrode configuration: a) the porous substrate conducts current; b) configuration with distal electrode [2]

2.5 Borosilicate glass

Coffman introduced commercially available porous borosilicate glass in order to overcome the limitations of the wet techniques, either chemical or electrochemical. These are given by spatial non-uniformity, non-repeatability and in the case of electrochemistry, the need for large driving currents [2]. The proposed method is laser ablation of borosilicate glass substrates. Layers of material are removed by scanning a laser beam across the surface of the substrate while periodically interrupting the beam resulting in the formation of emitter tips. The glass has a porosity of 40% and pore size varying between 2 and 5 μm. The measured performance of a thruster using porous borosilicate glass was presented in Table 1-1. The limitations of the porous glass are given by non-uniform pore size distribution. This method also poses a limit on densification due to the finite beam width of the laser. Figure 2-9 shows the particle size distribution of porous borosilicate glass and an emitter feature from a large array.
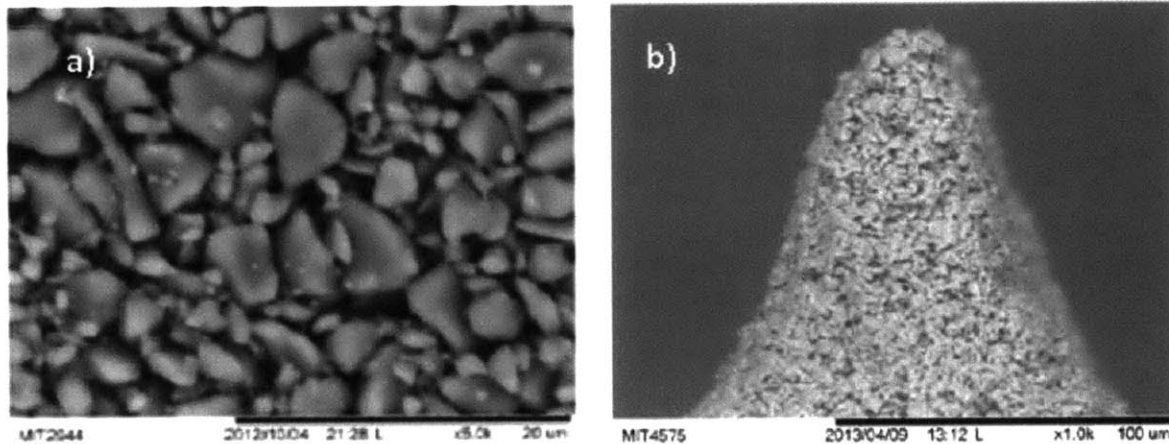
Figure 2-9 – a) Porous borosilicate glass with varying pore sizes; b) Emitter tip [2]

2.6 Sintered porous glass

In order to address the issue of batch manufacturing, which was not achievable with the previous substrates obtained via subtractive methods, Xie researched an additive method of fabricating emitter arrays. Soda lime glass microspheres are deposited into molds to form columns with diameters of 25 μm, 50 μm or 75 μm. They are then sintered to create a porous substrate which

31

becomes an emitter when the device layer is etched with XeF2. Xie tested a porous sintered glass piece shaped into an emitter. An emitted curent of 6 μA was obtained at an applied voltage of 2.5 kV [18]. A schematic of the fabrication process is shown in Figure 2-10.

The design of Xie relies on the previous research by Krpoun and Shea. However, instead of using non-porous capillary arrays filled with silica micro beads that would make for a porous bulk substrate, Xie relies on creating a porous emitter altogether. The soda lime microspheres were commercially available and composed of SiO_2, CaO, MgO, Na_2O, K_2O and Al_2O_3. The particles are polydisperse and have diameters between 2 μm and 10 μm. A picture of the microstructure of glass microspheres on top of a silicon surface can be seen in Figure 2-11 a). Xie attempted different sintering iterations and created an array of emitters with irregular features caused by the polydisperse particles and by their overflow onto the front side of the mold as seen in Figure 2-11 b). Variability across the array was observed, as tips appear to have different heights.
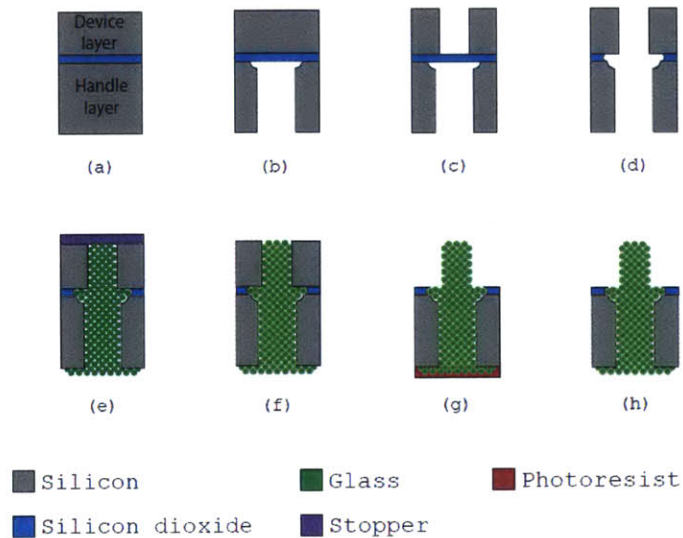
Figure 2-10 – Manufacturing process of sintered glass: a) Silicon on insulator (SOI) wafer; b) Deep reactive ion etching (DRIE) etches away material from the handle layer; c) DRIE etches away material from the device layer; d) etch of the buried oxide (BOX) layer; e) glass microspheres are deposited in the created mold; f) sintering process; g) XeF2 etches away the device layer h) emitters are created by removing a film protecting the handle layer [18]

32
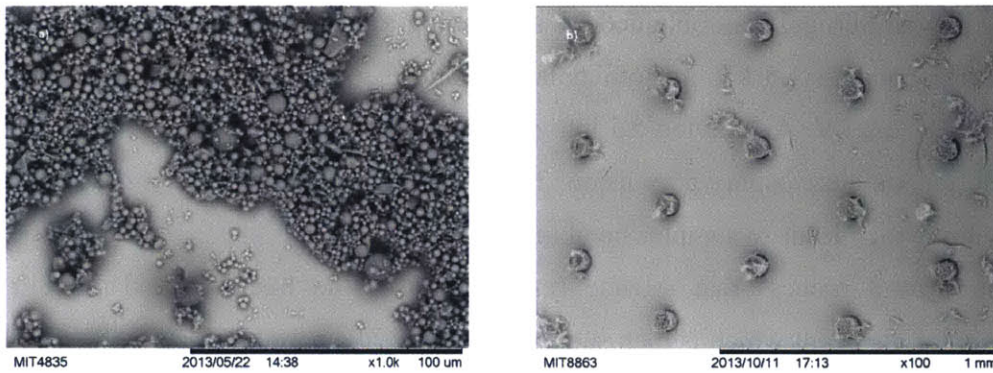
Figure 2-11 – Sintered porous glass: a) SEM image of soda lime spheres on top of a silicon surface; b) Array of emitters [18]

2.7 Alumina xerogels

At the same time as Xie, Arestie [19] focused on another additive method of fabrication using three processes: sol-gel, freeze-cast and sol-freeze. The sol-gel process will be explained in detail in the following chapter. With this process Arestie created Alumina xerogels following a recipe by Tokudume [20]. The advantage of this process is that it allows for pore size variations by changing the amount of catalyst. This translates into being able to obtain pure ionic emission by limiting the flow of propellant. The recipe includes the mixture of deionized water, ethanol, Polyethylene oxide (PEO), Aluminum chloride hexahydrate ($AlCl_3 \cdot 6H_2O$) and Propylene oxide (C_3H_6O) in the right amounts. Then the mixture is allowed to gel and cure. A monolith and the microstructure of the Alumina xerogel with pore size uniformity are shown in Figure 2-12.
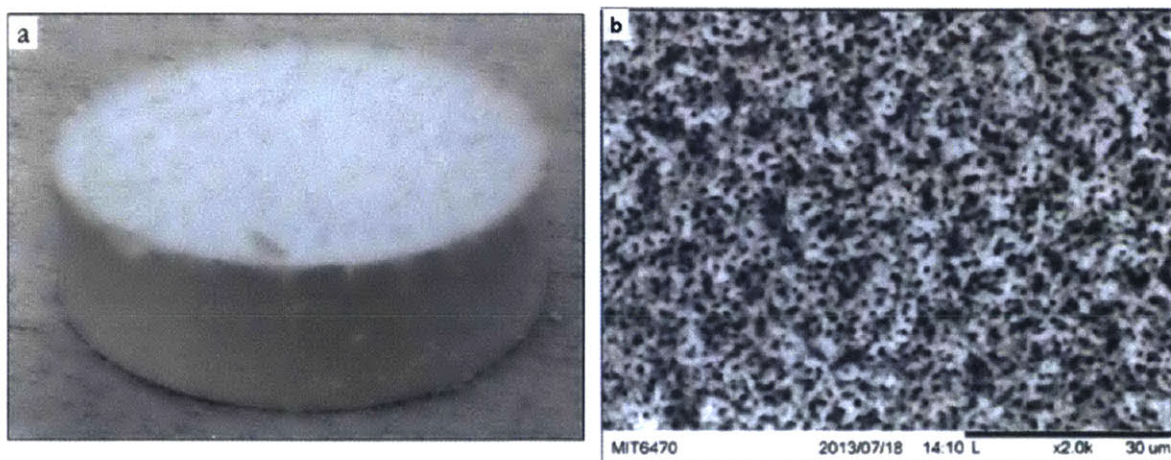
Figure 2-12 – a) Alumina xerogel monolith; b) SEM of Alumina xerogel [19]

A tip of Alumina xerogel was obtained by sharpening a piece of material and tested. Start-up voltages correspond to 1.5 kV in both polarities and 5 μA of emitted current correspond to voltages of ~+/- 2.2 kV. Arestie looked into molding arrays of Alumina but deemed the process not feasible for ion electrospray propulsion. The limitation he encountered is given by shrinkage during drying, which leads to samples breaking apart.

The second process that Arestie researched was the freeze-cast. This relies on the solidification of a solvent which is then sublimated to reveal a porous structure. Several iterations of different recipes were carried out, all containing a solvent (water or camphene), alumina powder or colloidal silica, and additives. Both slow and fast freezing rates were investigated when using the alumina powder. A first formulation for molding was attempted for slow freezing and structures with 250 μm diameter were obtained. Most features were replicated with little breakage but the pore size of the microstructure was much larger than what is desired for ion electrospray propulsion. Moreover, pores were dendrite shaped as their shape was given by the void left by the ice crystals. In order to attain a smaller pore size and uniform pores a second formulation of fast freezing was employed. The pores were no longer dendrite shaped but the pore size was still too big, with sizes on the order of tens of microns. A change in constituents produced smaller but non-uniform pores. This third formulation was employed to mold porous alumina in capillaries or into molding tips. The second and third formulations are presented in Figure 2-13.
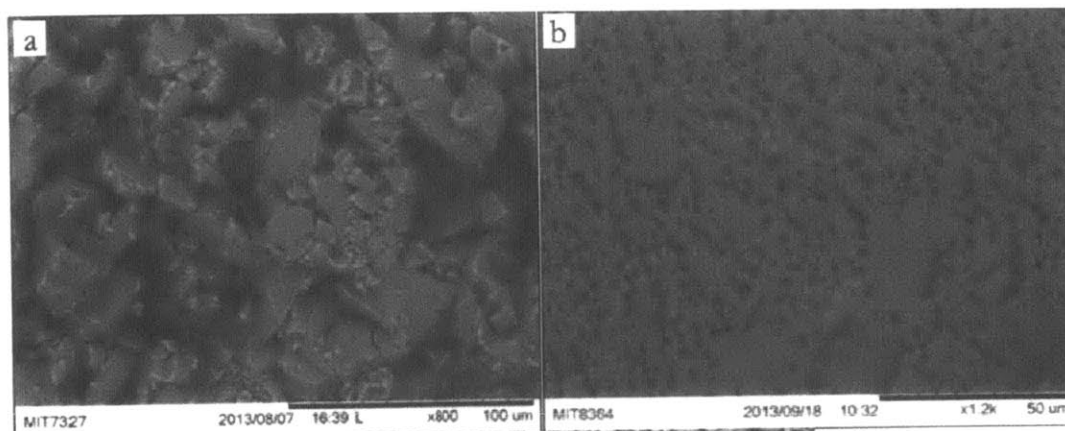
Figure 2-13 – SEM of freeze casted Alumina through formulations 2 and 3 [19]

34

The third process researched by Arestie was a combination of the sol-gel and freeze cast processes, named the sol-freeze method. It starts with the alumina xerogel obtained in the sol gel process and continues with grinding the monolith. The particles are then used in the freeze cast method instead of the nanopowder alumina. The goal of this method was to obtain uniform porosity even in the larger particles that are usually obtained from the freeze cast method and also to avoid shrinkage. Figure 2-14 shows a picture of the sol-gel microstructure. Arestie concluded that the process had to be more extensively explored and that it should eventually allow for molding micron size features with uniform porosity [19].
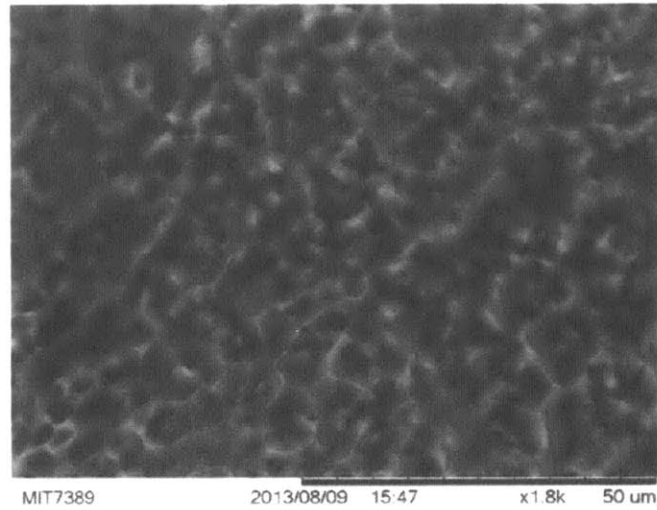
Figure 2-14 – SEM image of the substrate obtained via the sol freeze method [19]

Chapter 3

Technical approach

The ion electrospray emitter arrays can be created using two methods. The substrates can be created subtractively, for example with a laser beam that removes material from the substrate and interrupting the beam resulting in emitter tip geometries, or additively by molding. The ultimate goal of this research is to allow for parallel processing and batch manufacturing of emitter arrays. This can be achieved via the second method, that of molding.

Porous materials are ideal for ion electrospray propulsion due to their ability to transport the propellant via capillary forces. They provide both the emitter array structure and they have the function of transporting the propellant to emission sites [21]. When the porous material has a high enough hydraulic impedance that allows for very small ratios of flow to electrical conductivity, the pure ionic regime (PIR) can be obtained. This regime is of interest to this work as it produces high specific impulse [22].

The technical approach of this research is to investigate the use of carbon xerogels as emitter arrays for the ion electrospray propulsion system. The current challenges of the state of the art emitter arrays are given by non-uniform pores, pore size variability, non-uniform emitter tips, and difficulty in creating identical tips. The research goal is to create an emitter array with uniform pores, uniform and identical emitter tips and mechanical integrity. Initially carbon xerogels substrates are synthesized. Then a carbon xerogel emitter tip is molded on top of a previously synthesized carbon substrate. Finally, an array of resorcinol formaldehyde emitters is molded on top of a carbon substrate. The processes use a synthesis route which is much more advantageous for reproducibility than commercially acquired porous substrates.

3.1 Xerogel theory

Xerogels are materials with large internal void space, high surface area, low thermal conductivity, and high acoustic impedance. They are low density open-cell foams derived from

wet gels usually through the sol-gel process. They have applications in a variety of areas, from biology to aerospace engineering. The potential applications include thermal insulation, catalysts, gas storage and gas filters, acoustic materials, dielectrics and electrically conductive materials [23]. There are different types of xerogels and aerogels, the most common ones using inorganic metal or semimetal oxide frameworks [23]. Pekala developed the first purely organic aerogels which are based on the resorcinol-formaldehyde (RF) resin [24]. Subsequently other types of organic aerogels were developed based on formaldehyde resins such as melamine-formaldehyde, cresol-formaldehyde, phenol-formaldehyde, and others such as polyurethanes, polystyrenes, polyacrylates, polyimides, etc. [23, 25].

Resorcinol-formaldehyde (RF) aerogels can be synthesized by base or acid catalyzed polycondensation of resorcinol with formaldehyde in an aqueous environment. After supercritically or subcritically drying they are pyrolyzed in an inert atmosphere to produce the carbon aerogel or xerogel. Further thermal activation, usually in a CO_2 environment, provides access to higher surface areas by further opening up pores and by offering bimodal porosity (macro and micro pores) [26]. The amount and type of catalyst influence the size and shape of the particles within the network and therefore influence the structural properties of the resulting xerogel [26].

The xerogels obtained in this research are synthesized through the chemical process called sol-gel. The first stage of the process is associated with the preparation of a sol mixture in which particles form a colloid. The subsequent step is the gelation in which particles collide and attach to each other creating larger particles and ultimately a gel. The next step is the curing of the gel where more reactions occur. The last stage is given by drying of the gel. This can be done in air, in which case the product is a xerogel or in a supercritical drier and the product is an aerogel. The difference between the two is that the xerogel shrinks during drying while the aerogel does not. The formation of xerogels and aerogels is schematically shown in Figure 3-1.

The gel is a two phase material comprised of both a solid and a liquid. The solid represents the scaffold we are interested in preserving while removing the remainder liquid solution. Gelation times vary between different types of xerogels and coincide with the formation of the last links that create the whole structure within a container. More crosslinking occurs after gelation, during curing, which results in increasing the complexity and the stiffness of the xerogel. The xerogel may exhibit shrinkage during this step. Drying is the last step in which the

remainder liquid is removed. The xerogel exhibits most shrinkage during this step by an amount equal to the volume of the evaporated liquid. If shrinkage is not desired, supercritical drying can be employed, where the liquid is extracted before being evaporated [19]. Sintering or pyrolysis is the last steps in creating a xerogel and they are optional. Sintering is used for inorganic xerogels to further strengthen the created network. Pyrolysis is used for organic xerogels and impacts the structural and performance characteristics of the xerogel.
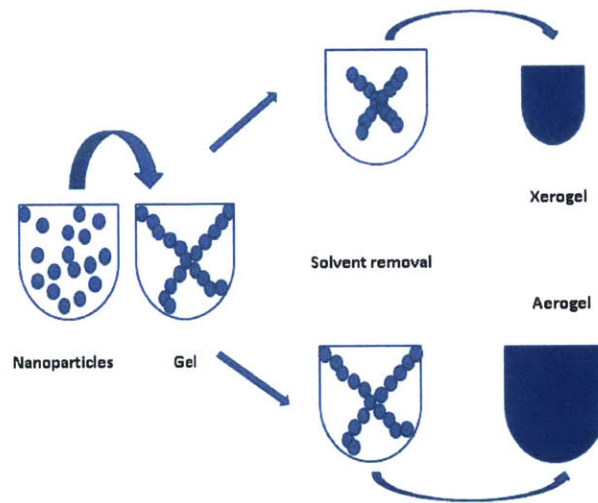
Figure 3-1 – The steps in the sol-gel process

3.2 Experimental process

For this research RF xerogels have been produced by mixing resorcinol (R) and formaldehyde (F) in the presence of acetic acid. This represents a polycondensation reaction in an acidic environment that leads towards the formation of molecular bridges towards a larger molecule, the xerogel. Acetic acid was chosen as catalyst due to its heritage in previous application employed by Baumann, Brandt and Arestie [26, 28, 19]. The most important factors that affect the properties of the organic gel are the catalyst concentration, the initial gel pH, the concentration of the solids in the sol and the drying procedure [24].

During the synthesis process 28 parts resorcinol and 41 parts 37 % formaldehyde solution are dissolved in 34 parts water. One part of acetic acid is then added. The process starts with

adding resorcinol in a beaker of deionized water and stirring the mix. The use of an ultrasonic bath can speed the process. The stirring should be done until the resorcinol is fully dissolved and this depends on the reactant amounts. During this step the beaker should be covered with parafilm to avoid evaporation. The subsequent step is the addition of the aqueous formaldehyde and stirring in the same ultrasonic bath. Acetic acid is added last and mixed thoroughly for one minute. The resulting solution is poured into molds.

Because the xerogel exhibits shrinkage the desired mold should be oversized. The mold should be as smooth as possible and should not react with the poured solution. For this research hydrophilic polydimethylsiloxane (PDMS) molds are used. PDMS is a non-toxic and biocompatible material used in microfluidic applications. It is easily fabricated, has optical transparency and elastomeric property and conveys a very high fidelity of the mold [29]. The synthesis route involves mixing of 53 parts of polydimethylsiloxane base and 5 parts curing agent. The addition of 1 part of polydimethylsiloxane ethylene oxide (PDMS PEO) produces a hydrophilic mold. It is observed during experiments that decreasing the content of the curing agent decreases the elasticity of the mold. It should be noted that molding of carbon xerogel substrates using hydrophobic PDMS was tested several times with no success. As the PDMS is hydrophobic the RF solution does not adhere to it perfectly when poured in the mold. As a result the created xerogel substrates do not have continuous straight surfaces, and also display holes. Therefore, all the molds that are used for carbon xerogel synthesis are created with hydrophilic PDMS.

After pouring the RF solution the PDMS mold is placed in a seal tight container and allowed to gel for 24 hours. The RF solution changes from transparent to opaque white and from liquid to gel. The opaque gel changes color into light orange. In the curing step the containers are moved to 40 and 60 degree ovens for 24 hours each and then to an 80-degree oven for 72 hours. During this time the RF turns into dark orange. The next step is drying of the gel. In this research drying is performed subcritically in ambient atmosphere and in the 80-degree oven. The supercritical method is not employed as this opens up and enlarges pores. This is not desired for ion-electrospray technology as we want to have very small pores on the order of 1 μm or less. During the drying step the containers are moved from the oven and allowed to cool. The container is subsequently opened and left unsealed in the fume hood for 24 hours. The last step involves moving the open container to the 80-degree oven for an additional 72 hours. The RF samples are then placed in a tube furnace and undergo pyrolysis in an Argon environment. The

samples are kept at 900 degrees C for 3 hours. The pyrolysis turns the RF polymer into a conductive carbon material.

The carbon samples exhibit shrinkage and deflection and also form a skin. These will be later discussed in the Challenges section. The carbon xerogel substrates are ground to the desired dimensions with high grit sandpaper and then polished using a six-micron grit diamond lapping film. These steps are performed in the fume hood. The samples are then cleaned in ultrasonic baths of acetone and isopropanol.

Every negative PDMS mold is created from a positive Aluminum mold. At first an Aluminum teeth-like mold was fabricated. This is dipped in a container of PDMS as seen in Figure 3-2 that cures to form the PDMS mold. The RF solution is then poured in the newly created PDMS mold. In this case the RF procedure creates a substrate that gels, cures and dries vertically. The samples obtained do not have uniform pore sizes as a gradient is observed from top to bottom. The upper part of the substrate which is in direct contact with the atmosphere also shrinks significantly more.
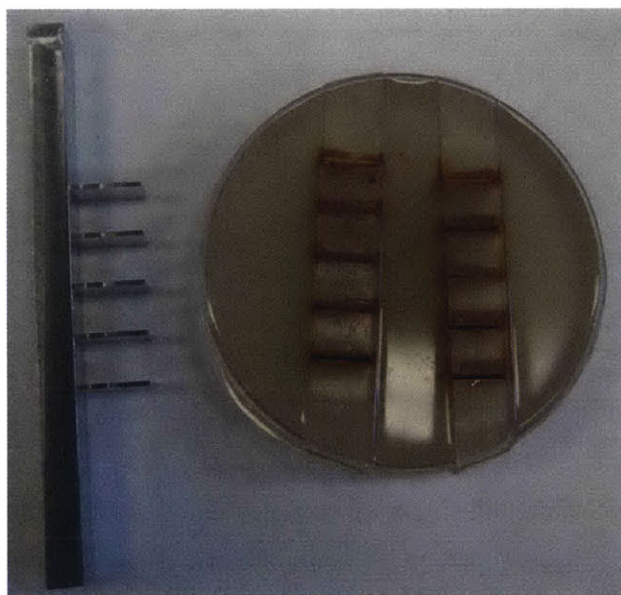
Figure 3-2 – PDMS mold first iteration: left - Aluminum mold with teeth-like structures with dimensions larger than the desired carbon xerogel substrates; right – cured PDMS mold obtained from dipping the Aluminum mold in the pre-cured PDMS - the pockets were filled with RF solution and RF xerogel substrates were obtained

Measurements of pore sizes from Scanning Electron Microscope (SEM) images taken for 2 substrates reveal that the pore size at the top (the warped part) of the substrate ranges from 10-12 μm, to 12-14 μm at the center and to 18-19 μm at the bottom. The pore size was also estimated by submersing the substrates in isopropanol and flowing nitrogen through them. Equating the pressure at which bubbles emerge from the substrate to the Young-Laplace pressure and assuming only spherical bubbles gives an estimate of the radius of the pores. The equation is given by

$$\Delta P = \frac{2\gamma}{R}$$

where γ is the surface tension of isopropanol and R the radius of the pores.

For carbon substrates obtained with this mold an average of 12 μm pore size was obtained at pressures ranging from 0.5 to 1.5 psi. However, the bubbles did not emerge uniformly from the substrate and a gradient was observed in this case also. A SEM picture of the carbon substrate is given in Figure 3-3.
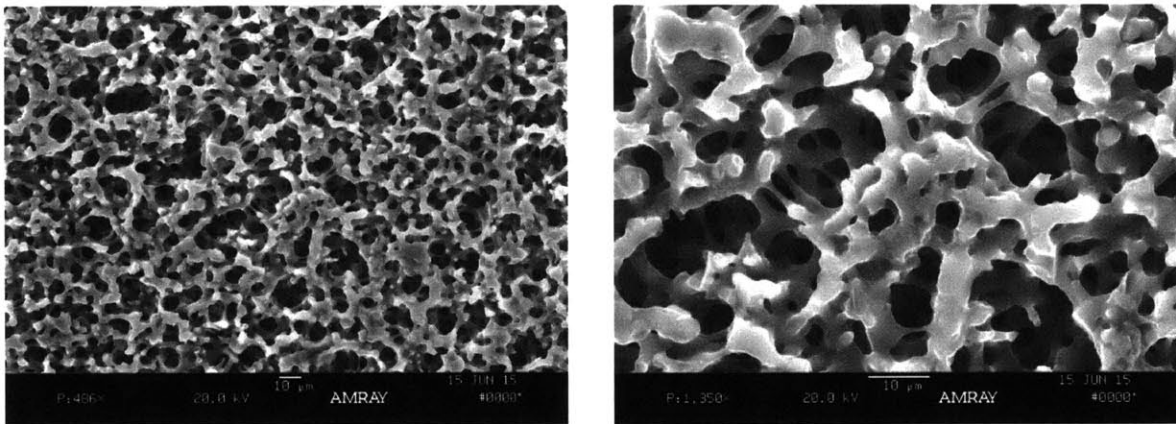
Figure 3-3 – SEM image of carbon substrate obtained via vertical molding process; the images are taken at the center of the sample and the second image represents a detail of the first image

An explanation to a gradient in pore size can be given by a differential rate of evaporation. The bottom of the substrate dries more slowly, meaning larger pores end up forming at the bottom. Here larger pores are analogous to larger crystals forming when a material is cooled more slowly.

A concave meniscus forms at the interface between the RF and the PDMS as seen in the xerogel substrate in Figure 3-4. A meniscus is a form of capillary action in which surface adhesion or internal cohesion pulls the liquid up or down. A concave meniscus forms when the particles of the solution are more attracted to the container than to each other. This causes the liquid to climb the walls of the container [30].

As the first iteration of the PDMS mold resulted in carbon samples with a gradient in pore size a second iteration PDMS and subsequently Aluminum mold were considered. The goal is to have the substrates gel, cure and dry horizontally and therefore avoid the vertical porosity gradient. An Aluminum mold with protruding features resembling the shape of the desired carbon substrates is fabricated as seen in Figure 3-5.

Figure 3-4 – Xerogel substrates: left side - RF xerogel substrate with meniscus forming at the contact of RF solution, PDMS mold and air; right side – the same substrate after pyrolysis

Figure 3-5 – Aluminum mold used for creating the PDMS mold

The PDMS is poured in the Aluminum mold to create a PDMS mold with pockets. The RF solution is poured in the pockets of the PDMS mold and allowed to gel, cure and dry through the previously stated process. The RF samples obtained are shown in Figure 3-6. The RF substrates are subsequently pyrolyzed and filed to the desired dimension. A substrate obtained via this method is shown in Figure 3-7.
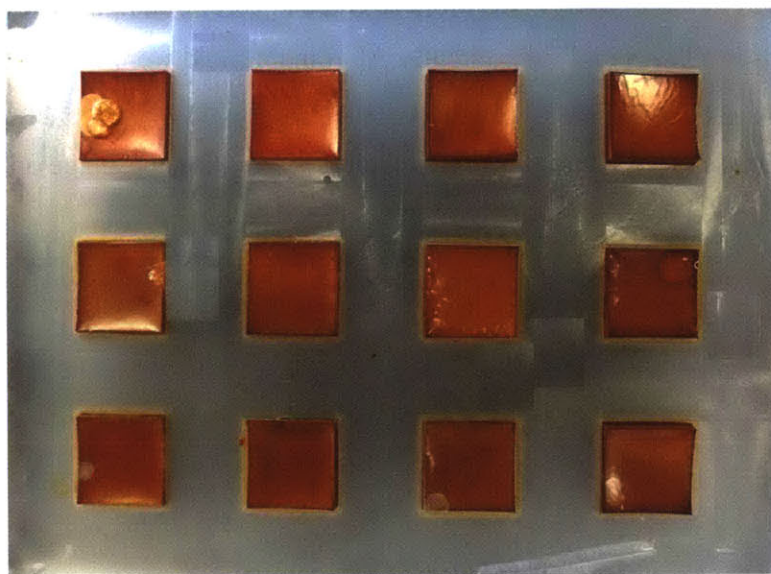
Figure 3-6 – PDMS mold with horizontally cured RF substrates
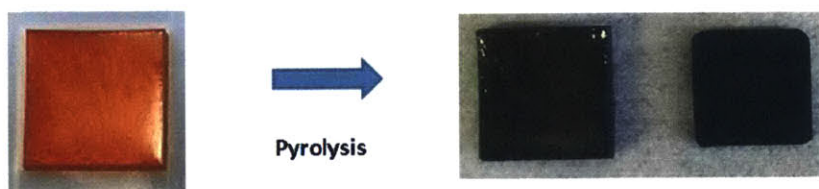
Figure 3-7 – RF substrate that undergoes pyrolysis and is shaped into the desired dimension

Shortening the process

As previously described, the process of creating carbon xerogels lasts for two weeks. In an attempt to shorten the process different gelling, curing and drying times are tested. Baumann's method states that shorter times can be implemented. In his method the RF solution is poured into

molds and allowed to cure for 72 hours at 80 degrees. The organic aerogel is then supercritically dried with CO_2 and subsequently pyrolyzed at 1050 degrees C in a nitrogen environment for 3 hours [26]. For this research the first process of obtaining RF xerogel allows gelling for 24 hours in the fume hood and curing for 72 hours in the 40, 60 and 80 degrees ovens, for 24 hours each; drying is performed for 24 hours in the fume hood and for 72 hours at 80 degrees. It is observed that gelling takes place in the first 18 hours, when the substrates turn opaque white. Curing follows in the next 24 hours, when the samples turn orange. The new process last for four days and it involves keeping the samples for 18 hours in the fume hood, for 6 hours at 40 degrees C, for 18 hours at 60 degrees C and for 30 hours at 80 degrees C. This process was refined by Jimmy Rojas-Herrera [31]. The RF substrates undergo the same pyrolyzation process. The carbon xerogels obtained with this process have pore sizes of ~1 μm. A SEM picture of a carbon substrate obtained via this process is shown in Figure 3-8. The measurements from the image reveal that the pore sizes are on the order of 1 μm. Pressure burst tests result in pore sizes of 1 μm as well.
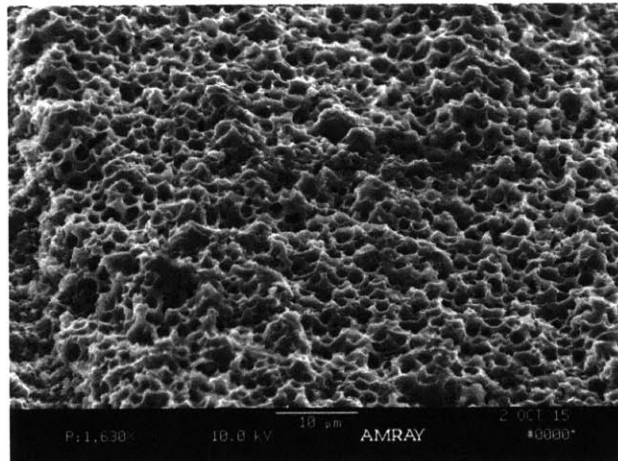
Figure 3-8 – SEM picture of a carbon substrate obtained with the four-day process [32]

3.2.1 Creating a carbon substrate with a molded emitter tip

In the previous section it was demonstrated that carbon substrates can be synthesized. The goal of the research is to allow for batch manufacturing and parallel processing and this can be obtained with an additive technique. In order to achieve this, molding of one emitter tip on a carbon

substrate is attempted. The carbon substrate acts as a porous scaffold through which the ionic liquid is brought to the emission site by capillary forces and the tip represents the emission site.

Creating the mold represents the initial step. First, a negative Aluminum mold is fabricated. This is filled with PDMS to create a positive PDMS mold. The PDMS mold is first covered with parafilm and then punctured from above with a tungsten needle. The tungsten needle has a radius of curvature of 10 μm and half angle of 20 degrees [33]. The tungsten needle is obtained through electrochemical etching of tungsten. The puncture is done from above, the base of the needle going into PDMS, as we want to keep the tip of the tungsten needle clean. The tungsten needles are previously cleaned in acetone and isopropanol baths for fifteen minutes each. The tungsten needle is now embedded in the PDMS mold with only about 1-2 mm sticking out. On top of this mold with a sticking needle, PDMS is poured once again and left to cure. The role of the parafilm is to separate the two PDMS molds which sit on top of each other and can fuse together during the second PDMS curing process. We are left with a new PDMS mold (the negative) which has a square form with dimensions slightly larger than the carbon substrates and with a tiny tip hole in the middle. The process is described in Figure 3-9.

A few drops of the RF solution created with the 4-day process are poured into the tiny hole of the PDMS mold that has the shape of the tungsten needle. Then a carbon xerogel substrate synthesized via the same synthesis route is placed in the PDMS mold. The carbon xerogel substrate is previously saturated with the RF solution until the pores are filled with liquid. This step in employed because otherwise the RF solution that fills the needle-like hole would be absorbed by the substrate itself. The carbon substrate and the PDMS mold are held together with a C-clamp, to ensure perfect contact between them. Then they are transferred to air-tight containers and the RF gelling, curing and drying process begins. A picture of the C-clamp holding together the carbon substrate and the PDMS mold is shown in Figure 3-10.

The newly formed substrate with the molded tip has a layer of RF on the side that was in contact with the PDMS. This thin layer is called a skin and will be discussed in the Challenges section. It is believed that the RF skin is not at the same scale as the porous bulk as it is tested for leaking with the pressure burst test described earlier and no bubbles emerge. The highest pressure achievable with the laboratory equipment is 33 psi. At this pressure there are no bubbles emerging from the substrate.
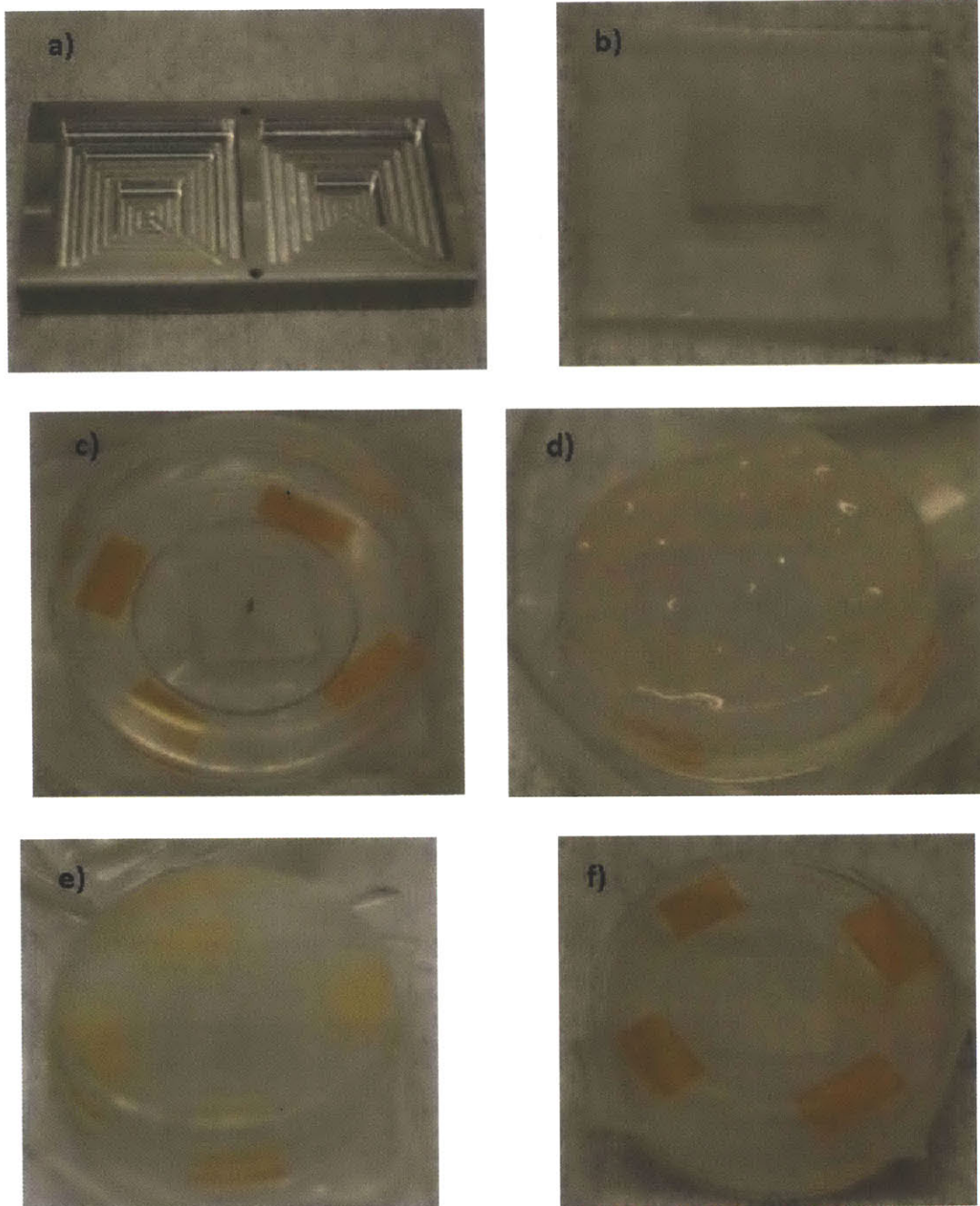
Figure 3-9 – Creating the mold for the single emitters: a) Aluminum mold (positive); b) PDMS mold (negative); c) PDMS mold (negative) covered with parafilm and punctured with a tungsten needle; on top of the parafilm sits a cut-out petri dish; d) the new PDMS is poured into the petri dish; e) the second PDMS procedure after curing; f) the negative PDMS mold obtained that has the form of a slightly larger square substrate and of a tip in the middle

Figure 3-10 – C-clamp holds together the carbon substrate and the PDMS mold

By equating the pressure at which bubbles emerge from the substrate to the Young-Laplace pressure and assuming only spherical bubbles, a 33 psi pressure results in pore sizes of ~ 0.4 μm. Therefore, if the skin is porous it must have pore sizes smaller than this value. Subsequently, the carbon substrate with the molded tip is pyrolyzed. The substrate undergoes pyrolysis a second time. The pressure burst test is performed again and it shows various results. For the first substrate which is used for the experiments presented in Chapter 5, the test does not reveal the flow of nitrogen through the substrate up to the 33 psi. However, for a second substrate with a molded tip the pressure burst test revealed bubbles emerging from the substrate at 17 psi. This translates into pores with sizes of 0.8 μm. Bubbles do not emerge from the tip itself from either substrate. This can be explained by the fact that once bubbles burst there is flow and the pressure goes down, so it becomes harder to force a burst in smaller pores.

The experimental results are presented in Chapter 5. A carbon substrate with a molded tip is shown in Figure 3-11.
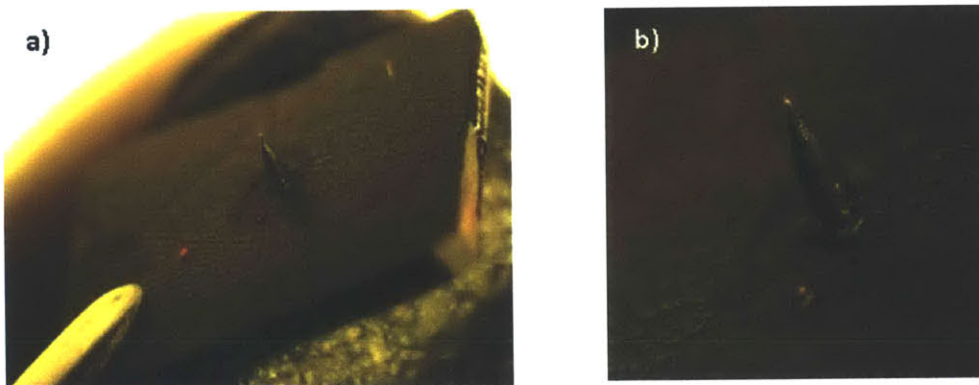
Figure 3-11 – Carbon molded tips: a) carbon substrate with molded carbon tip; b) detail of the carbon tip

48

SEM images of the substrate are shown in Figure 3-12. The first image represents the tip and the following three are details of the tip. From the first detail, which is taken at the base of the tip, it can be inferred that pores exist. However, this is not confirmed by the pressure burst tests as bubbles do not emerge from the tip. The next two details are from the top of the tip and reveal a rough surface. This morphology of the emitter is similar to the one of the tungsten needle, which is electrochemically etched in order to have a non-smooth surface. This characteristic enhances the wetting capabilities of the needles with ionic liquids. If the tungsten needles are smooth then the liquid does not reach the top of the tip.
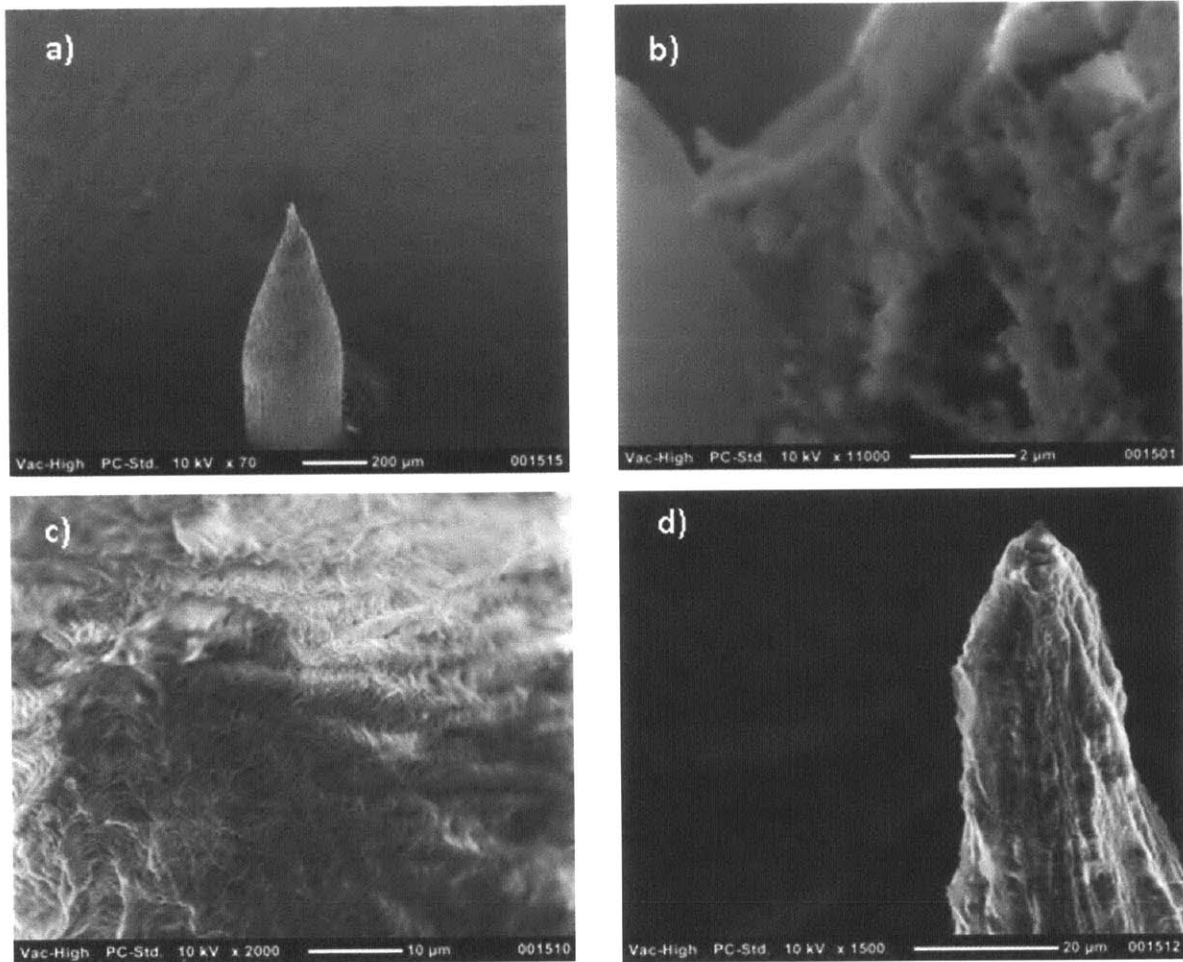
Figure 3-12 – SEM photographs of molded tips: a) SEM picture of the carbon tip molded on the carbon substrate; b) detail from the base of the carbon tip that seems to have pores; c) and d) detail from the top of the carbon tip

3.2.2 Molding carbon/RF arrays

The goal of the research is to create arrays through an additive process. The process uses the same two-step RF procedure described earlier. First, carbon xerogel substrates are synthesized, pyrolyzed and shaped to the desired dimension. Then a mold for creating the array is fabricated. The mold starts with a porous borosilicate emitter array obtained through laser ablation. This is the shape that we want to replicate and to create a PDMS negative mold with. The process starts with using a·similar PDMS negative mold as in Figure 3-9 c). On top of the PDMS we put a layer of parafilm and then a borosilicate glass substrate and a cut-out petri dish. PDMS gel is poured in the petri dish and cured. The newly created PDMS mold (negative) has array-like features on the bottom. A picture of a borosilicate glass emitter array and the resulting PDMS mold are shown in Figure 3-13. It is important to note that the borosilicate glass is porous and the resulting PDMS mold is also porous local to the surface. This results in demolding issues of the PDMS from the borosilicate glass and later of the RF array from the PDMS. To overcome this, the borosilicate glass is coated with a layer of Teflon. The layers have thicknesses of 70 nm, 105 nm and 140 nm. Experiments show that a thicker layer of Teflon works best for demolding.
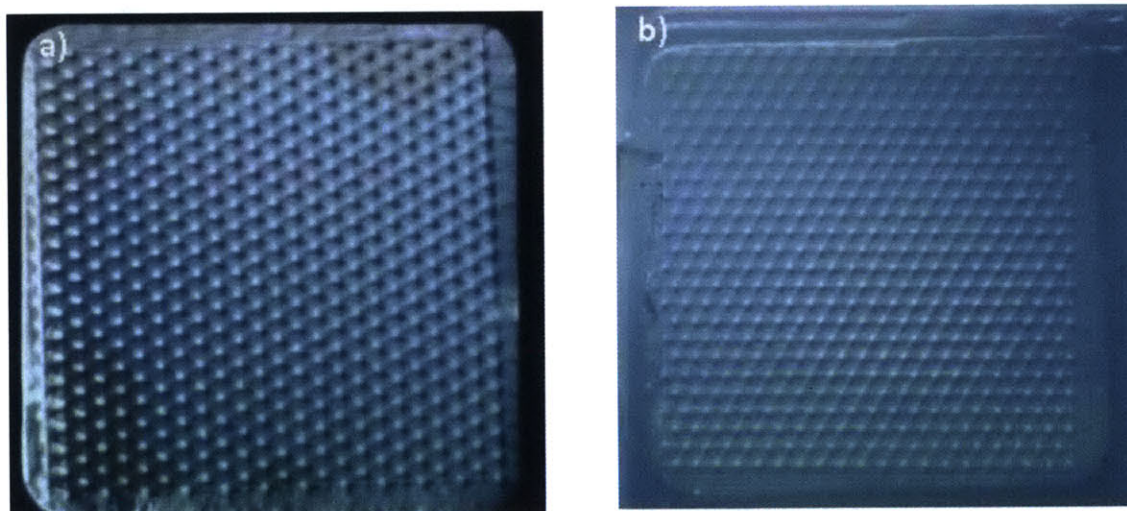
Figure 3-13 – a) a borosilicate emitter array; b) a PDMS mold obtained from the borosilicate emitter array

Several carbon xerogel substrates with RF emitter arrays are created. The first carbon array is created with a PDMS mold obtained using a glass substrate that is coated with a layer of 70 nm

thick Teflon. The carbon array and SEM images are presented in Figure 3-14. In the first image PDMS is sticking on top of the RF emitters as demolding is not perfect. This hints that the PDMS mold is porous and RF cures inside the pores as well. The following three images are SEM pictures of the substrate.

The second and third arrays together with their SEM images are presented in figures 3-15 and 3-16. As the thickness of the Teflon layer is increased demolding is easier as less PDMS adheres to the RF emitters. The Teflon layer for the second array is 105 nm thick and for the third array 140 nm thick. Traces of PDMS are still present in the second and third array. It should be noted that demolding issues should not occur if the positive mold that is used to create the negative PDMS mold is not porous.
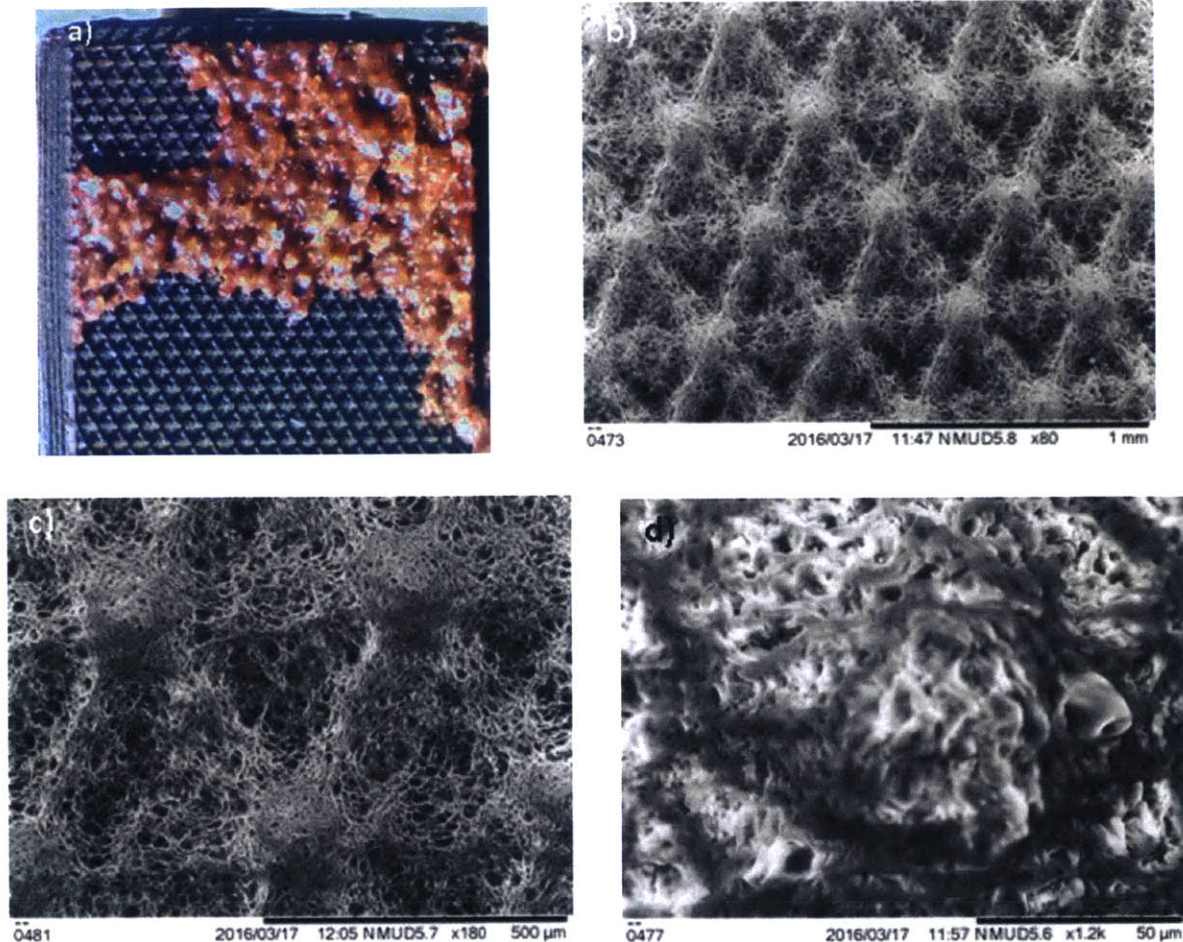
Figure 3- 14 – a) microscope image of a molded RF array of emitters on a carbon substrate; b) and c) SEM images of the array; d) detail of a single emitter
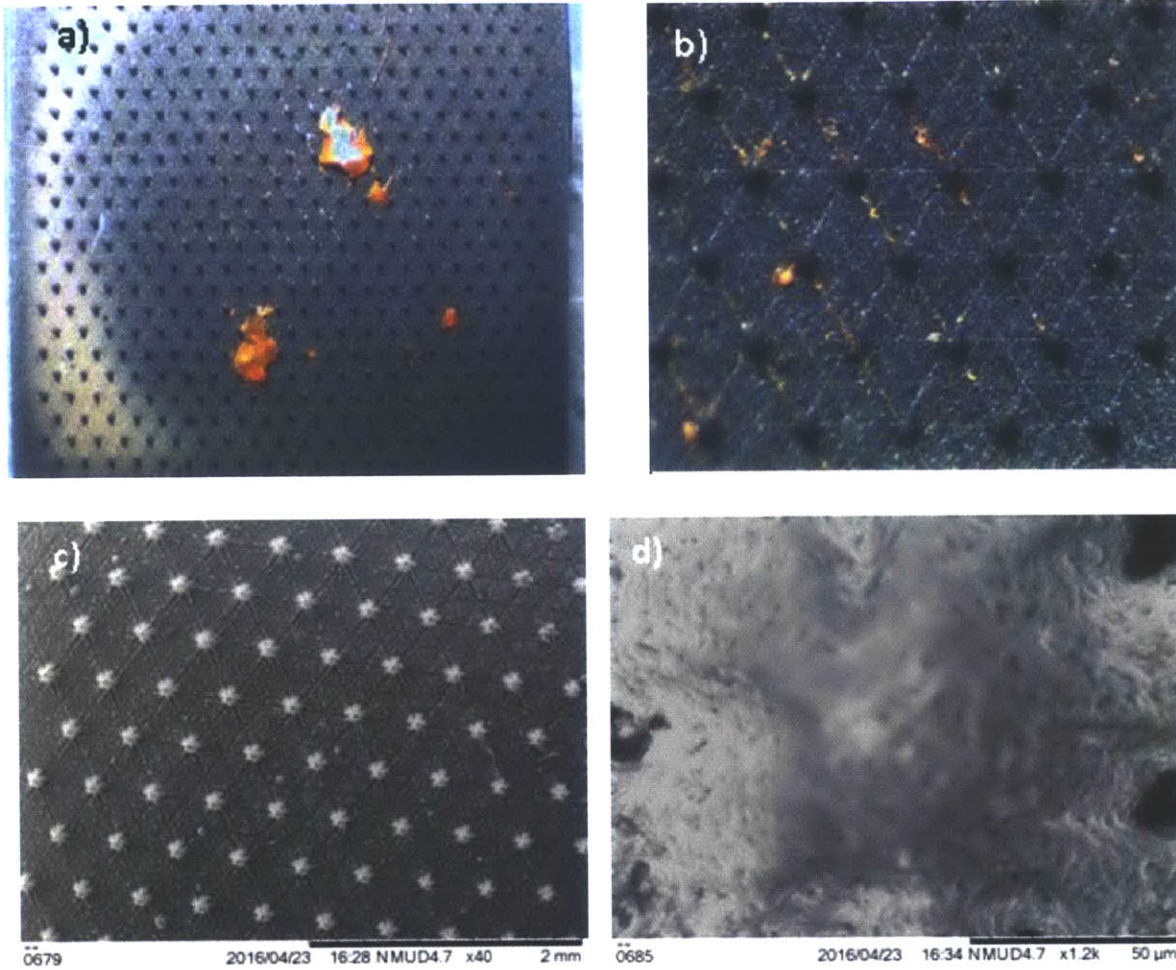
Figure 3-15 – a) and b) microscope images of the second molded RF array on a carbon substrate; c) and d) SEM images of the array with a detail of a single emitter
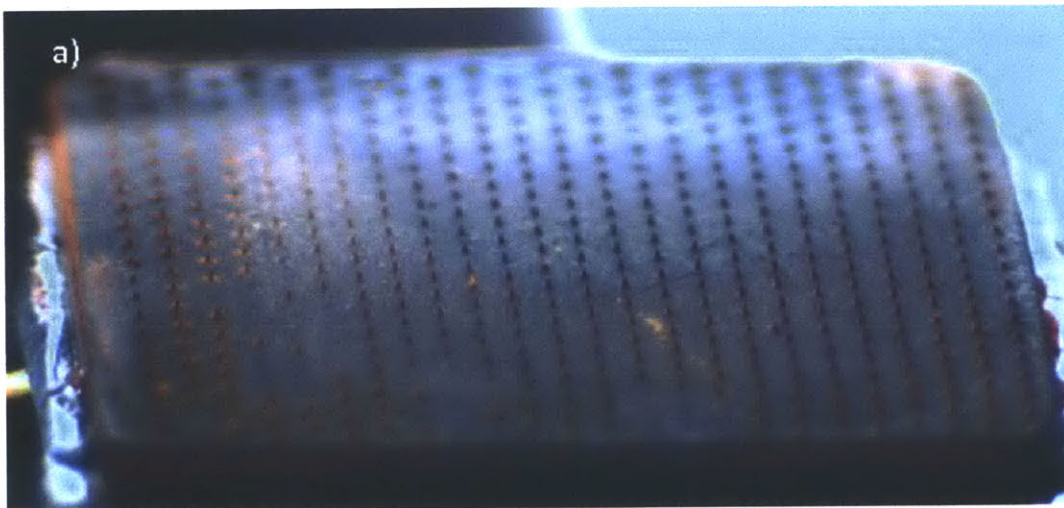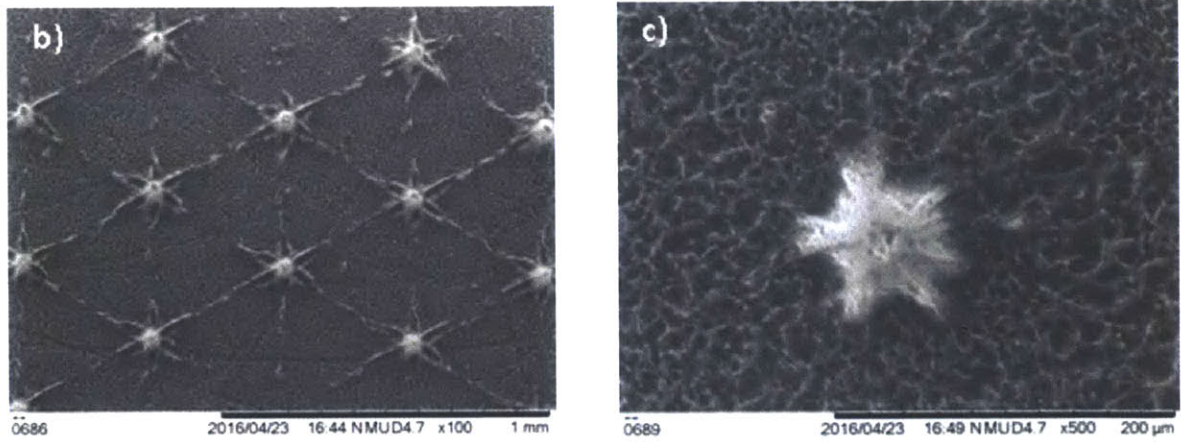
Figure 3-16 – a) microscope image of the third molded RF array on a carbon substrate; b) and c) SEM images of the array with a detail of a single emitter
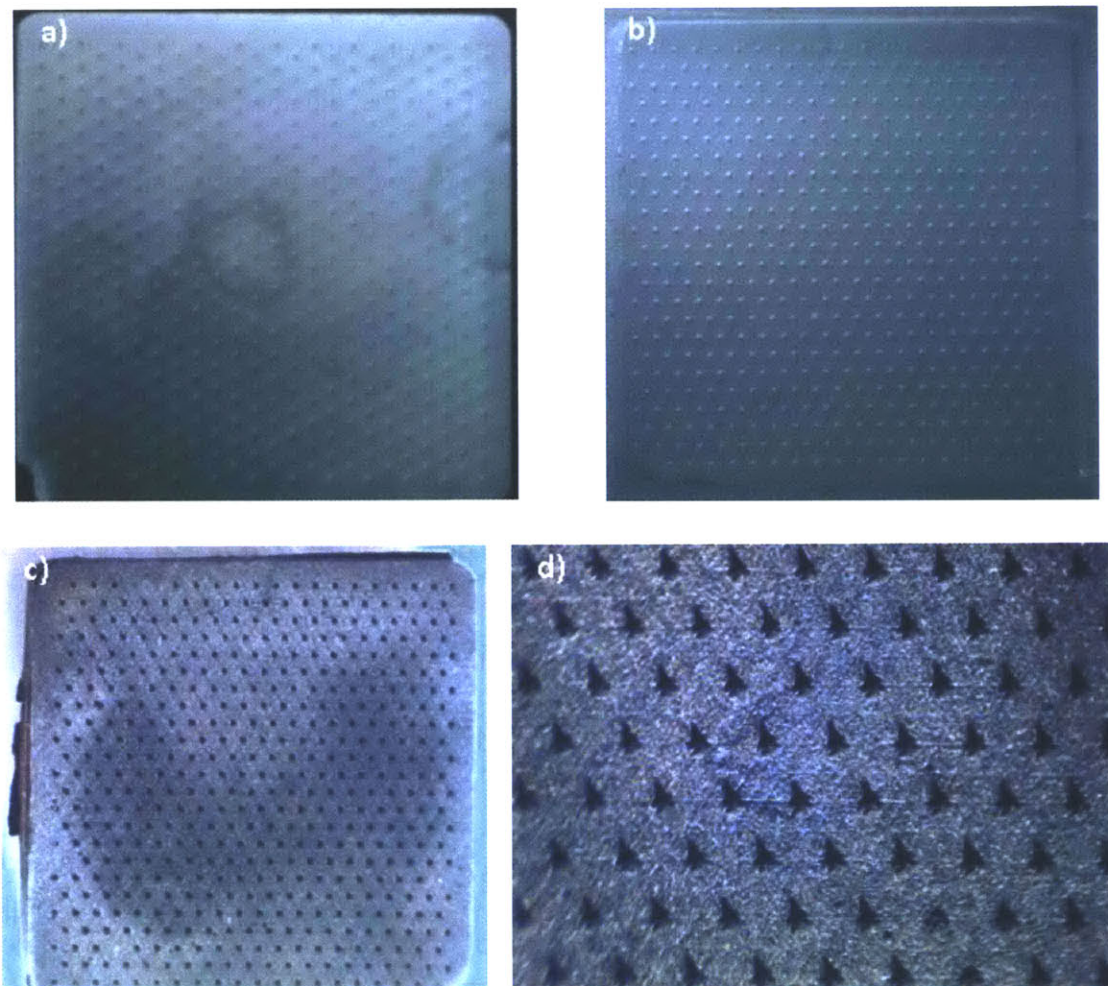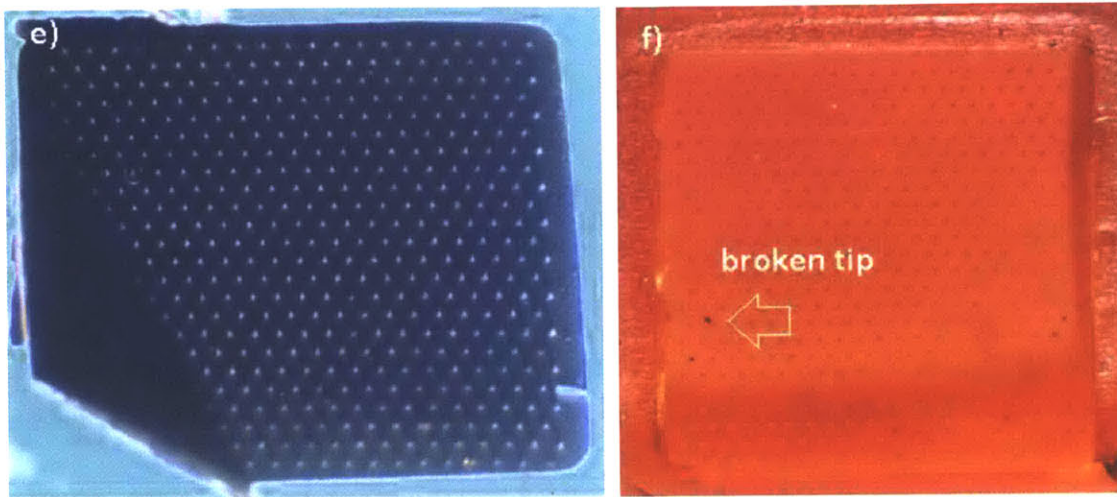
Figure 3-17 – a) glass array; b) PDMS mold obtained from the glass array; c) carbon array obtained from the PDMS array; d) detail of the carbon array; e) side view of the carbon array – the light in the lower left side is blocked as the substrate is held with tweezers; f) the PDMS mold after RF curing – it displays very few broken RF tips that did not demold properly

Removing the PDMS chemically is not attempted in this research. Work by Dahyia [34] states that PDMS can be removed chemically from nano-structures. The author uses a dilute solution of tetrabutylammonium fluoride (TBAF) 1% in a hydrophobic nonhydroxylic aprotic solvent (propylene glycol methyl ether acetate (PMA)) to etch PDMS from Si wires.

A fourth carbon xerogel array is molded by using the PDMS reactant ratios: 263.15 parts base solution, 21.05 parts curing agent and 1 part PDMS PEO. The glass array is coated with 140 nm Teflon as in the third molded carbon array. The RF process is the same as the four day process with the specification that the container is left open in the 80 degree oven for three additional days. The demolded carbon array does not display PDMS residue and only a few tips are broken at demolding. The glass array, the PDMS mold and the carbon array are presented in Figure 3-17.

3.3 Challenges

The challenges encountered in using the resorcinol formaldehyde synthesis procedure are represented by skin formation, shrinkage and deflection of substrates.

3.3.1. Skin formation

The skin is a thin layer formed on the surface of the RF xerogels that is different than the bulk. Experiments and SEM images show that the skin could be non-porous or has smaller pores than the rest of the substrate. Moreover, the skin appears to be thicker on the surface of the substrate that is in contact with the atmosphere. One of the explanations could be that at the interface with air the water evaporates more quickly and causes the pores to close. This could also be backed up by the first RF experiments in which larger pores formed at the bottom of the vertically synthesized substrates. Petricevic [35] concluded that skin formation depends on surface/volume ratio (S/V), which represents the reciprocal mean distance between two adjacent surfaces. For hydrophilic surfaces, at very low S/V ratios the influence of the hydrophilic surface is negligible. As the ratio of S/V becomes on the order of the inverse of the catalytic penetration depth (λ) the influence of the surface becomes more prominent until we are left with only a skin attached to the surface. The diagram in Figure 3-18 explains the different cases of aerogel deposition. The generalized surface is the contact surface between the sol and the boundary. The main conclusion is that when molding very small features in carbon using a hydrophilic mold there exists the possibility of having only skin and no xerogel. This is an important conclusion that helps understanding the microstructure of the molded carbon tips in an array.
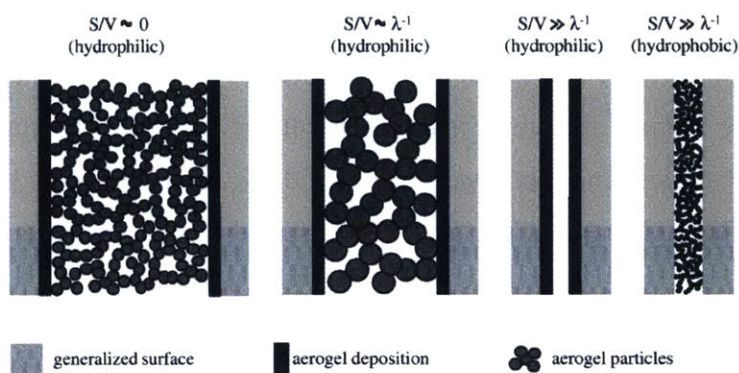
Figure 3-18 – Skin formation: for $S/V \approx 0$ the surface has no influence on the gel structure; for $S/V \approx \lambda^{-1}$ the sol is diluted and the RF reactants are consumed via surface deposition forming larger particles that delay gelation; for $S/V >> \lambda^{-1}$ the catalytic influence of the surface is present in the entire volume of the sol and a hydrophilic surface causes deposition while a hydrophobic surface causes build-up [35].

The formation of the skin can be seen in the SEM picture in Figure 3-19. The bottom of the first image reveals a porous substrate while the top seems to have closed pores or very small pores not distinguishable with the SEM. The same is valid for the second picture, but this time the pores are at the top of the image.
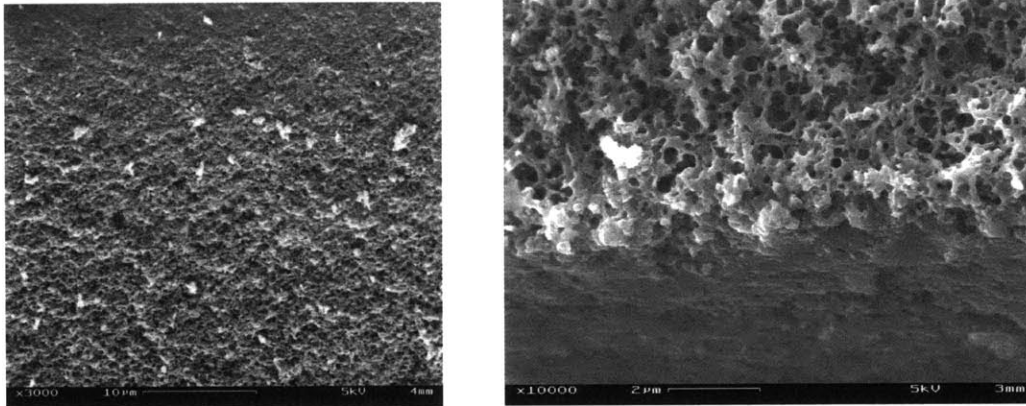
Figure 3-19 – SEM images revealing skin formation (2 week process)

Wetting and absorption experiments with the ionic liquid EMI-BF$_4$ of pyrolyzed substrates reveal different results. Out of 10 pyrolyzed samples (that underwent the same RF synthesis and pyrolysis) eight absorbed the ionic liquid on the top surface (the one that is in contact with the atmosphere during RF curing). An ionic liquid drop is absorbed very fast (in ~5 s) for five samples or slower for the other three (~1 h). The bottom sides (which are in contact with the PDMS mold) also absorb the ionic liquid but at lower rates (observed qualitatively after eight hours for two of the samples that absorbed the ionic liquid in ~5 s). This reveals that the skin is porous for these substrates. The other two samples did not absorb the ionic liquid on their top or bottom surfaces (after eight hours). The liquid drop spreads on the top surface of one of the two substrates revealing a contact angle close to zero. The liquid drop on the bottom of the second sample has a contact angle of ~ 30 degrees. This hints that the top skin is different from the bottom skin. The differences in absorption could be attributed to the flow of argon in the tubular furnace not being perfectly laminar in all the regions (but at the limit between laminar and turbulent) and interacting differently with the samples, to a gradient of temperature in the ovens (the flow in the ovens could produce a horizontal gradient) or to the chemicals. The synthesis route for this experiment used the four-day process. The experiment should be repeated and the samples should also be characterized with the SEM.

3.3.2 Shrinkage and deflection

The substrates shrink during curing and drying and during pyrolysis. Measurements reveal that the shrinkage exhibited from evaporation is 10 %. During pyrolysis, in which hydrogen and oxygen are removed, the samples shrink by 19 %.

Deflection is also observed in carbon substrates. Deflection is prominent at the surface of the RF substrate that is in contact with the atmosphere. A picture of a warped carbon xerogel is given in Figure 3-20. Deflection can be caused by a differential rate of evaporation, as the bottom and sides of the substrate dry more slowly resulting in the formation of larger pores. This leads to less shrinkage at the bottom and subsequently to warping. Another explanation of warping could be attributed to a gradient of temperature across the solution. This could affect the rate at which the solid forms and therefore lead to deflection.
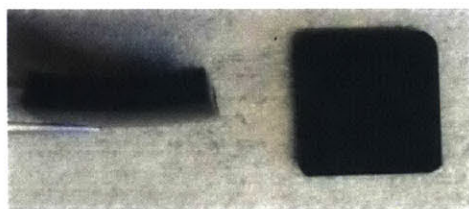
Figure 3-20 – Warped carbon substrate as obtained through the RF process and pyrolysis (left); final shape of the substrate after filing (right)

The warping is the reason for which carbon arrays cannot be created in a one-step process. Molding a substrate with a tip in one process was attempted but the resulting substrate on which the tip is sitting is warped. A picture of the RF substrate and a detail of the tip are given in Figure 3-21.
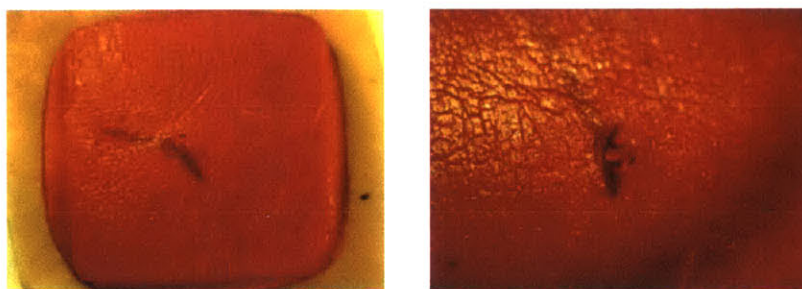
Figure 3-21 – One step process of synthesizing a RF substrate with a tip in which deflection of the substrate is visible; the right image represents a detail of the tip

The goal of the two-step process is to have a perfectly flat substrate with emitters on top. It is very important to note that when molding tips on carbon substrates only shrinkage is observed in tips and no warping. This may be due to the fact that the molded tip is not in contact with the atmosphere. A picture of a broken tip in its PDMS mold is shown in Figure 3-22 where shrinkage of the tip is visible.

Shearing is also believed to take place when molding a tip or an array on a carbon substrate. The tips go through synthesis and pyrolysis once, while the substrate undergoes pyrolysis twice. The shrinkage of the substrate is different than the shrinkage of the tip. The substrate is pyrolyzed so there is probably negligible shrinkage during the tip synthesis process. The tip shrinks on the order of 10 % over the course of solidifying and on the order of 20 % during pyrolysis.
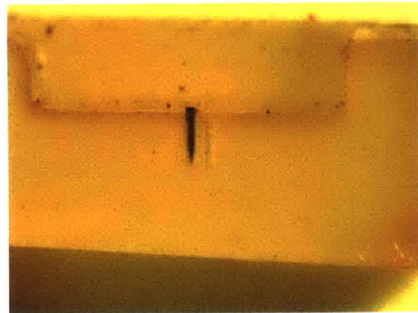
Figure 3-22 – A broken RF tip in the PDMS mold; shrinkage of the tip is visible especially at the top of the tip

Chapter 4

Experimental methods

The carbon substrate with the molded tip presented in the previous chapter was fired in order to measure fragmentation fractions and the beam composition. The first experimental technique is the Retarding Potential Analyzer (RPA) that probes the energy of the beam. This reveals the fragmentation fractions for break up in the acceleration region and in field free space. The second technique is the time of flight mass spectrometry (TOF) which yields the beam composition. The ionic liquid EMI-BF$_4$ is used as propellant and the emitter voltage is biased +/- 1400 to +/- 1800 V. The emitter voltage is biased across a range in which the emission current is stable. The extractor hole size is ~1.6 mm and the extraction distance is ~200 microns. The experiments are carried out in the MIT Space Propulsion Laboratory Minivac vacuum chamber shown in Figure 4-1. The chamber has two 140 l/s turbo molecular pumps. The pressures range from 10−5 Torr to 10−7 Torr.
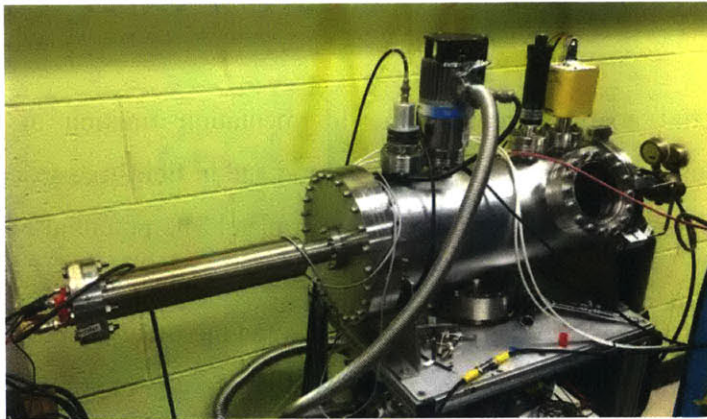
Figure 4-1 – The Minivac Vacuum Chamber at MIT Space Propulsion Laboratory

The experimental setup involves mounting the carbon substrate with a molded tip using ev plates, which are the stainless steel plates shown in Figure 4-2 . The substrate is sitting on a base ev plate and is held in place by another ev plate fixed on top of the substrate with teflon screws. The extractor grid is represented by a third ev plate with a 1.6 mm aperture which is mounted on top. The tip of the carbon substrate aligns with the hole of the extractor grid. The alignment is done

manually with the aid of a flashlight. Figure 4-2 shows a photograph of the carbon substrate setup without the extractor plate on the left and with the extractor plate on the right. The carbon tip is visible in the left picture.
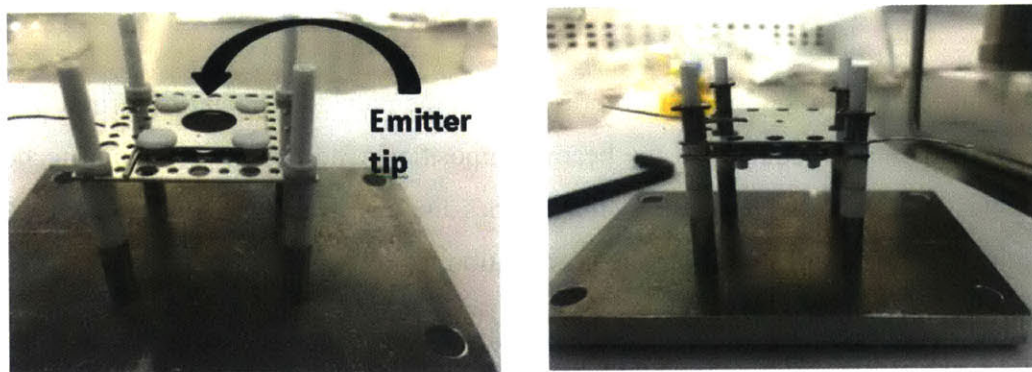
Figure 4-2 – Setup of the carbon substrate; left - the carbon substrate is integrated with ev plates; right - the extractor grid with 1.6 mm aperture is placed on top

4.1 Retarding Potential Analysis

The retarding potential analyzer reveals the fragmentation fraction of solvated ions. The fragmentation can occur in both the acceleration region and in field-free space. The setup consists of several grids placed in front of a current collecting plate. The potential of the carbon substrate is biased using a high voltage power supply and the extractor plate is grounded. The front grid of the RPA is grounded to ensure there is no current between the tip and the detector. The voltage is varied continuously from 0 to 1.2 times the source voltage for the next set of grids. These are the retarding grids. Ions are stopped when they reach a voltage in the grids that is equal to their kinetic energy. The last grid is placed in front of the collector plate and is used to repel any secondary electrons. It is called the electron repelling grid. The secondary electrons are created when ions impact the metal surface of the collector plate. The RPA used in this research is spherical.

4.1.1 RPA Theory

The ions that result from fragmentation events are called broken ions and they have kinetic energies less than the applied voltage. The kinetic energy of the broken ion depends on the place where fragmentation occurs, in the acceleration region or in field free space. If the solvated ion breaks up in field free space it is no longer accelerated and therefore the velocity of the broken ion is the same. However, the mass of the broken ion is less than that of the solvated ion and its kinetic energy decreases as well. The kinetic energy of a broken ion in field free space is [36, 37]:

$$K_{bi} = \frac{m_i}{m_{pi}} q_i V_0$$

where m_i is the mass of the broken ion, m_{pi} is the mass of the parent ion, q_i is the charge of the broken ion and V_0 is the applied potential. An ideal RPA scan with no fragmentation is presented in Figure 4-3 (left). The beam is monoenergetic. Fragmentation of dimers into monomers in field free space is shown in Figure 4-3 (right). Current is plotted as a function of voltage. The collected current is normalized by the maximum current and the retarding voltage is normalized by the source voltage. The height of the step at m_i/m_{di} represents the percentage of the total current that corresponds to fragmented dimers into monomers.
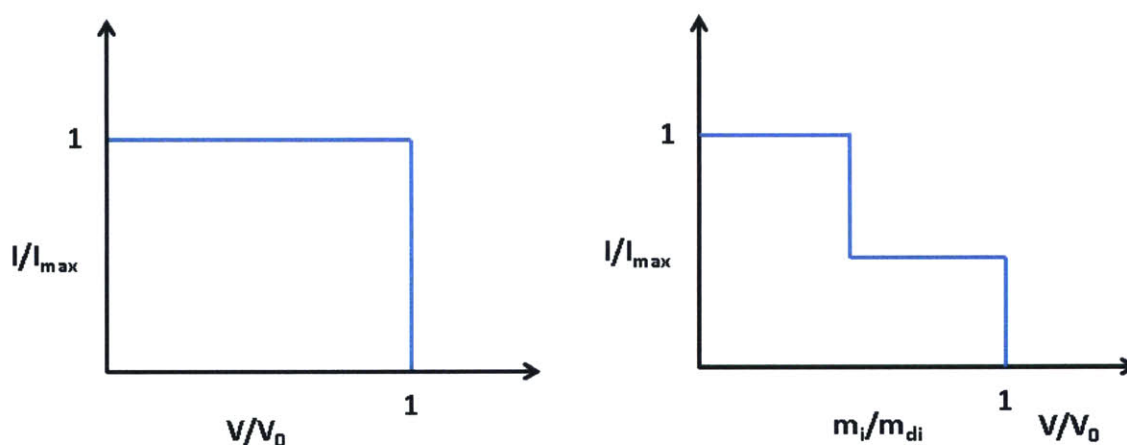

Figure 4-3 – RPA scan for a monoenergetic beam (left) and RPA scan for fragmentation of dimers into monomers (right), both in field free space [36, 38]

The kinetic energies of broken ions resulting from fragmentation in the acceleration region have a range of velocities. This is because the ions are still accelerated. The kinetic energy of the broken ion is given in this case by [36, 37]:

$$K_{bi} = q_i \left(\frac{m_i}{m_{pi}} - 1 \right) V_B + q_i V_0$$

where m_i is the mass of the broken ion, m_{pi} is the mass of the parent ion, q_i is the charge of the broken ion, V_0 is the applied potential and V_B is the local value of the potential where the solvated ion breaks up. This value of kinetic energy is always larger than the kinetic energy for free space and always less than the applied voltage. Figure 4-4 shows an ideal scan for fragmentation in both the acceleration region and in field free space. Fragmentation in field free space has sharp vertical slopes while fragmentation in the acceleration region displays slopes at angles different from vertical. The slope is not a straight line when the break up is not uniform in potential in the acceleration region.
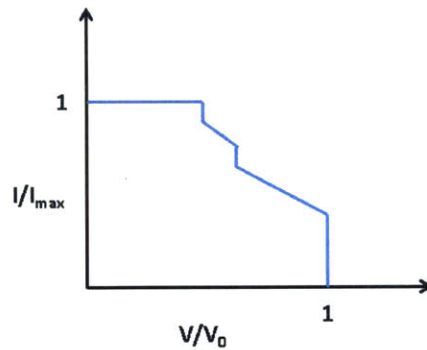
Figure 4-4 – Fragmentation in both the acceleration region and field free space [36, 38]

4.1.2 RPA Experimental facility

A spherical RPA was used to measure the beam current because the beam spreads spherically and ions have their kinetic energies within a solid angle. A diagram of the RPA is shown in Figure 4-5.
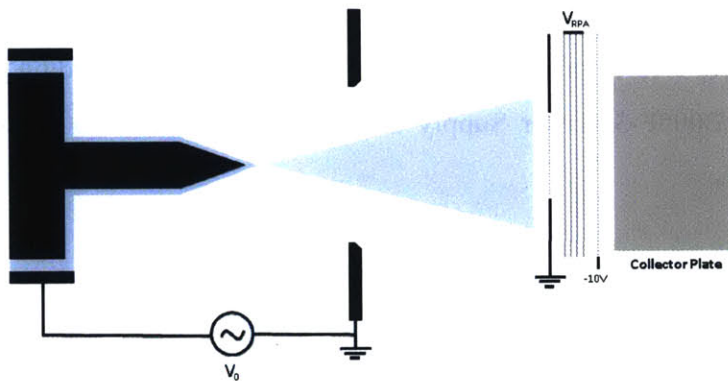
Figure 4-5 – Retarding Potential Analyzer Diagram

The grounded grid and the electron repelling grid are coarser than the retarding grids. The grids are made from stainless steel. Figure 4-6 shows a picture of the spherical RPA.

Figure 4-6 – Spherical RPA

The equipment used for these experiments is the following:

- Keithley 428-PROG Current Amplifier used for amplifying the current collected by the collector plate
- Matsusada AMS-5B6 High Voltage Amplifier used for supplying high voltage to the RPA grids
- Agilent Infinium 54835A Oscilloscope used to measure the output of the current amplifier and retarding voltage signals

- Agilent 33220A Signal Generator used to control the waveform of the high voltage amplifier and to create a high voltage triangular wave for the retarding grids
- DC RSR HY3005F-3 Power Supply used to supply voltage to the secondary electron repelling grid.

4.2 Time of Flight Mass Spectrometry

The ion beam is nearly monoenergetic if no fragmentation occurs. There always exists a very small energy spread. The beam consists of monomers and solvated ions which have the same energies but different masses. The ions have therefore different velocities and their identity can be revealed by measuring their flight time along a predetermined distance. The composition of the ion beam and the fragmentation fraction of each species in the acceleration region can be determined with time of flight spectrometry. This is done by measuring the current collected by a detector at a distance from the emitter as a function of time. The velocity of the broken ion depends on where in the acceleration region the fragmentation takes place. Fragmentation occurring near the emitter gives higher velocity than fragmentation occurring towards the end of the acceleration region. Therefore, the broken ions have a spread in final velocities.

4.2.1 TOF Theory

The velocity of an electrostatically accelerated ion that is not produced by a fragmentation event is given by:

$$v_i = \sqrt{\frac{2\,q_i V_0}{m_i}}$$

where q_i/m_i is the charge to mass ratio and V_0 is the source potential. The time of flight of the ion along a measured path can be calculated with:

$$t = d \sqrt{\frac{m_i}{2 \, q_i V_0}}$$

If the ion is produced by a fragmentation event it has a different velocity than above. The velocity of the broken ion is given by [36]:

$$v_{bi} = \sqrt{\frac{2 \, q_i V_0}{m_i} \left(1 - \frac{V_B}{V_0}\left(1 - \frac{m_i}{m_{pi}}\right)\right)}$$

Which results in the time flight of the broken ion:

$$t_{bi} = \frac{d}{\sqrt{\frac{2 \, q_i V_0}{m_i}\left(1 - \frac{V_B}{V_0}\left(1 - \frac{m_i}{m_{pi}}\right)\right)}}$$

Monomers are the fastest ions so they arrive first at the detector plate. Dimers have a slower velocity and arrive at a later time. If fragmentation occurs, a monomer resulting from a dimer in the region closer to the emitter tip will have a higher velocity than a monomer resulting from fragmentation farther in the acceleration region. Both monomers resulting from fragmentation have velocities slower than a normal monomer. An ideal time of flight scan for a monoenergetic beam is shown in Figure 4-7.
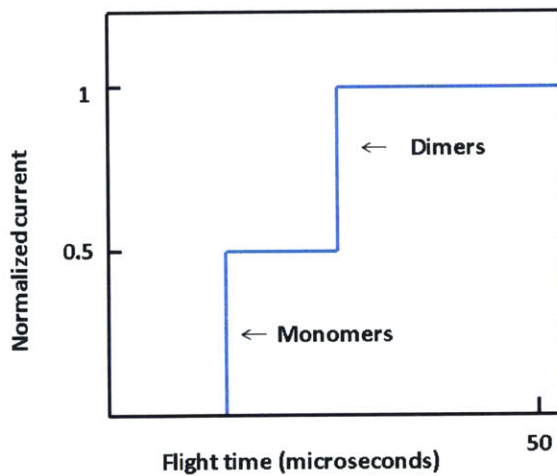

Figure 4-7 – Ideal Time of Flight Measurement for a Monoenergetic Beam [36]

65

The beam composition is given by the current fractions, with both monomers and dimers consisting 50 % of the beam. Figure 4-8 shows the effect of a uniform fragmentation of dimers into monomers in the acceleration region.
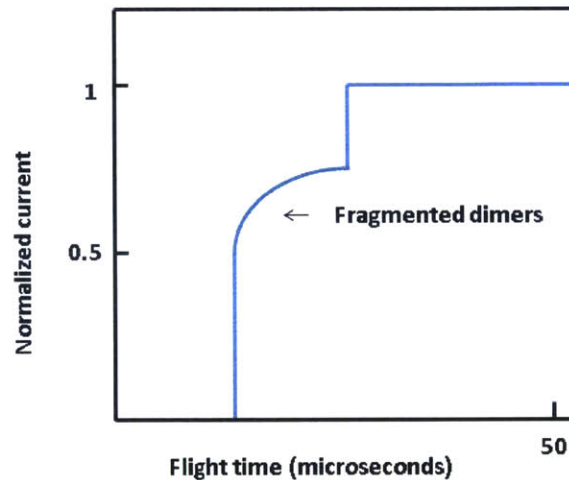

Figure 4-8 – Ideal Time of Flight Measurement with Fragmentation [36]

4.2.2 TOF Experimental facility

The experiment consists of an ion source represented by the emitter tip, a gate used to interrupt the beam, and a collector (detector) plate used to measure the current. A diagram of the setup is shown in Figure 4-9.

If the gate is closed the beam is interrupted and the detector does not measure any current. if the gate is open the detector measures the time of flight signal. The signal is averaged over many cycles by periodically interrupting the beam. The collector plate is a Channeltron Electron Multiplier with a very high gain, so even if the current input is very low, the output is high enough to be measured. The output signal from the detector is amplified with an amplifier before an oscilloscope reads the signal. The gate is a deflector gate that uses deflector plates biased to high voltage. This turns the beam away from the detector. The electron multiplier emits electrons when a particle collides with its surface. The multiplier uses tubes coated with silicon oxide, a material that produces electron when particles collide with the interior surface of the tube. The electrons are accelerated down the tube by applying a strong electric field and they produce more

electrons when they hit the walls. This creates a cascade of electrons that increases the current and allows for detection of low currents [36].
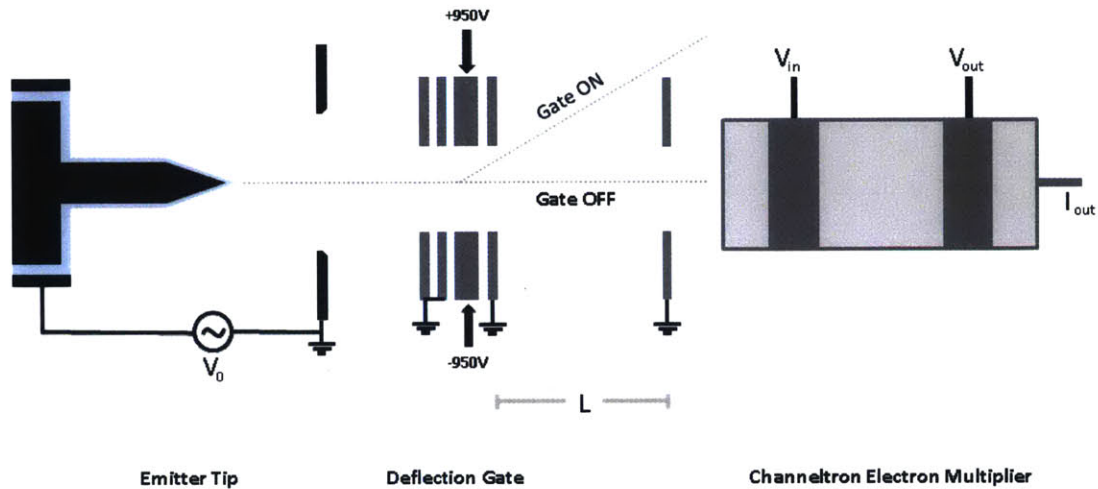

Figure 4-9 – Diagram of Time of Flight Detector

A pulse generator powered by an Acopian Power Supply acts on the gate. A signal generator controls the signal for the pulse generator. Several high voltage power supplies provide high voltage for each deflector plate. Another high voltage power supply supplies the high voltage to the Channeltron. The output of the Channeltron is read by an amplifier and then sent to the oscilloscope. The instruments required for time of flight measurements are the following:

- Agilent Signal Generator 33220A used to control the gate signal
- DEI Pulse Generator PVM-4210 used for the gate plates
- Acopian DC Power Supply BG25G30 used to supply voltage for the pulse generator
- Matsusada AMS-5B6 used to supply high voltage to a set of deflector plates
- Acopian High Voltage Power Supplies (positive PO3.5HP17 and negative NO3.5HP17) used to provide high voltage for two deflector plates
- Bertran High Voltage Power Supply 230-05R used to provide high voltage for the Channeltron
- Amplifier used to amplify the output signal from the Channeltron
- Agilent Oscilloscope Infiniium 54835A used to measure and record the Channeltron output signals

67

Chapter 5

Results and Discussion

The carbon xerogel substrate with the molded tip was tested with the ionic liquid EMI-BF$_4$ using the RPA and TOF experimental facilities in order to probe the fragmentation fractions and composition of the beam.

5.1 Current – Voltage curve

Current – voltage curves are taken to determine the stable range of operation. Figure 5-1 shows a current – voltage curve averaged from five curves. Emission starts with the formation of a Taylor cone. The waveform is triangular with a 200 s period and sweeps from -1600 V to 1600 V. The start-up voltage is 1.82 kV which results in a spike at 200 nA. Once the Taylor cone is formed the start-up voltage lowers to 1.2 kV (~30 nA emitted current) for the positive mode and -1.26 kV (~30 nA emitted current) for the negative mode. The emitted current is the measured supply current drawn by the emitter and the intercepted current is the current measured from the extractor electrode to ground. Relative interception is defined as the ratio of intercepted current to emitted current. At an emission current of 416 nA the intercepted current is 22.2 nA and at an emission current of -416 nA the intercepted current is -25.37 nA. The relative interception is 5 % and subsequently 6 %. This is consistent with the relative interceptions of laser ablated carbon arrays at 200 μA (6 %) and -174 μA (3.95 %) [39]. The ~ 400 nA values is selected as it represents the current for a single emitter in a laser ablated carbon xerogel array with 480 tips. The emission data shows relatively good symmetry for emission in both polarities.

The data processing cuts the voltage into periods because the voltage is not ideal so the voltage peaks do not necessary have the same values. Identical voltage levels are needed on all periods in order to compare the same values of output current. Binning is performed on cuts (e.g.: for values of voltage between 1595 and 1600 V, we assign the value of 1597.5 V). A voltage mean and a current mean are performed from 5 cuts which results in the average current-voltage curve.
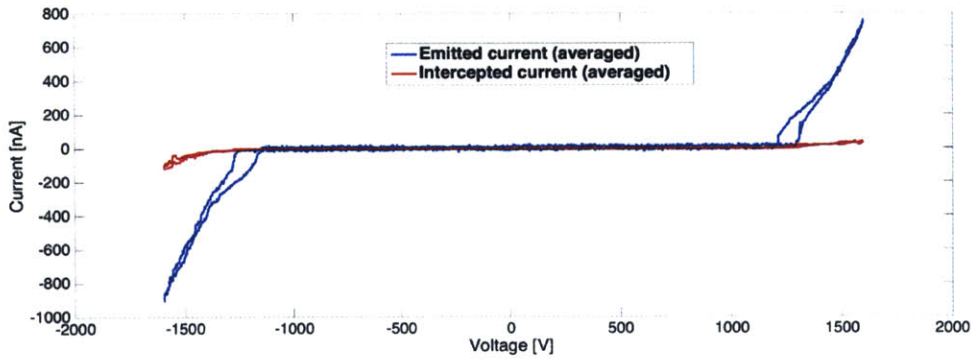
Figure 5-1 – IV curve

A second current-voltage curve is performed with the same single emitter carbon substrate previous to the RPA and TOF experiments. The start-up voltage is 1.6 kV for the formation of the Taylor cone and then it lowers to 1.2 kV. The source voltage and current measurements are shown in Figure 5-2. The current – time plot shows the existence of noise for voltages lower than the start-up voltage. This is an anomaly created by the HV Power Supply which does not supply a linear voltage to the emitter but a voltage with steps that produce spikes in current. The single emitter carbon substrate is placed on a metallic plate and the system acts as a parallel plate capacitor between the substrate and the grounded extractor. As the source voltage changes, a capacitive current can be created.
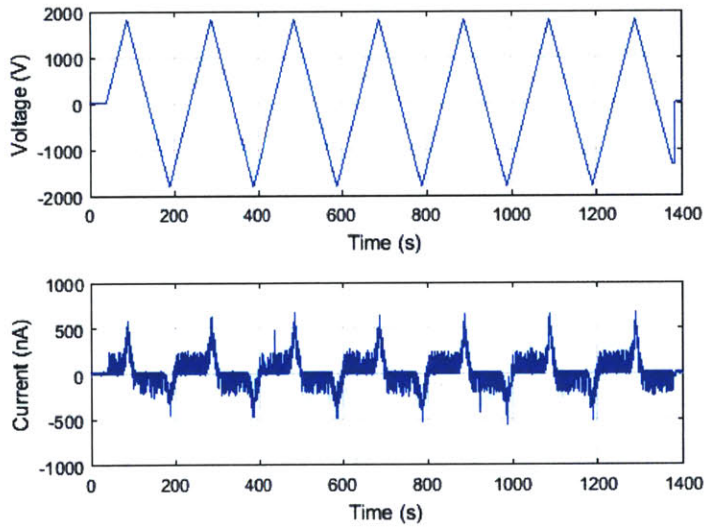

Figure 5-2 – Source Voltage and Current as a function of time

70

In order to remove the noise, the data is smoothed with a moving average. The voltages range from -1800 V to 1800 V. Figure 5-3 shows the second IV curve.
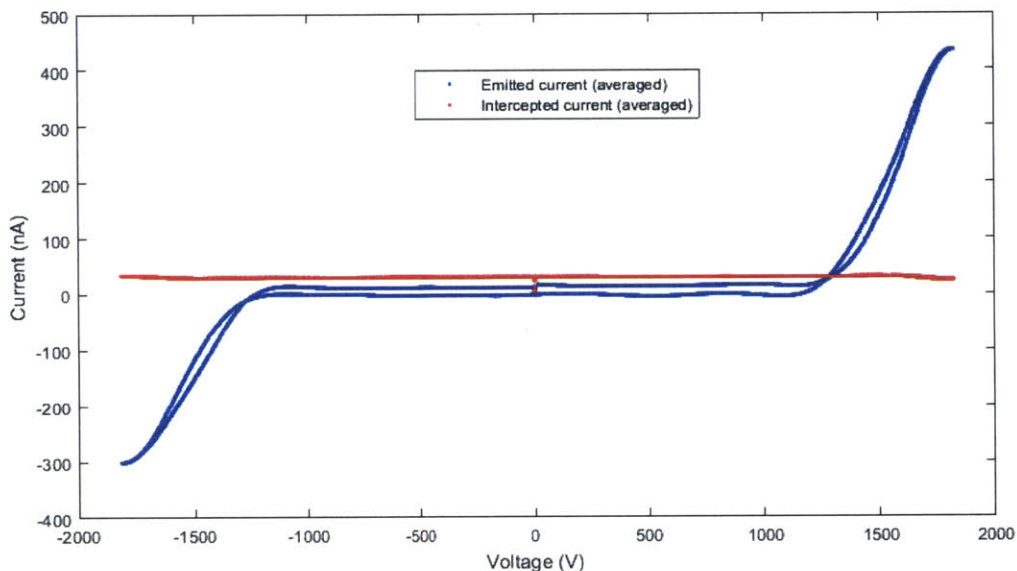

Figure 5-3 – Second IV curve

5.2 Retarding Potential Analysis

The retarding grid voltage is varied using a triangular wave with a 10 s period and the electron repelling grid is set to -30 V. Every scan of the oscilloscope includes two RPA scans, one for when the potential of the retarding grids is increasing and one for when the potential of the retarding grids is decreasing. There are several data processing steps for recording the beam fragmentation. The time varying voltage on the retarding grids creates a capacitive current which is removed by recording a scan for when the source is off. This is the baseline current which is subtracted from the recorded current. The voltage is normalized by the averaged source voltage and the current is normalized by the averaged source current. A RPA scan for 1400 V source voltage is shown in Figure 5-4. The normalized current is decreasing at normalized voltage values of approximately 0.36 and 0.6. This is consistent with the EMI-BF$_4$ dimer and trimer

fragmentation fractions. The mass of a positive ion is 111 AMU and the mass of a negative ion is 87 AMU. Therefore, for the positive mode the calculated dimer to monomer fragmentation fraction is 0.359 (= 111 / (111 x 2 + 87). The trimer to dimer fragmentation fraction is 0.609 (= (111 x 2 + 87) / (111 x 3 + 87 x 2)) which is also consistent with the plot. The figure also shows that the beam is close to monoenergetic as the steps are nearly straight and this corresponds to fragmentation outside the acceleration region. Fragmentation outside the acceleration region is desired as this does not affect the thruster efficiency. The increase in the normalized current as the normalized voltage approaches 1 is an anomalous feature caused by the RPA. The averaged emitted current at 1400 V is 69.95 nA.
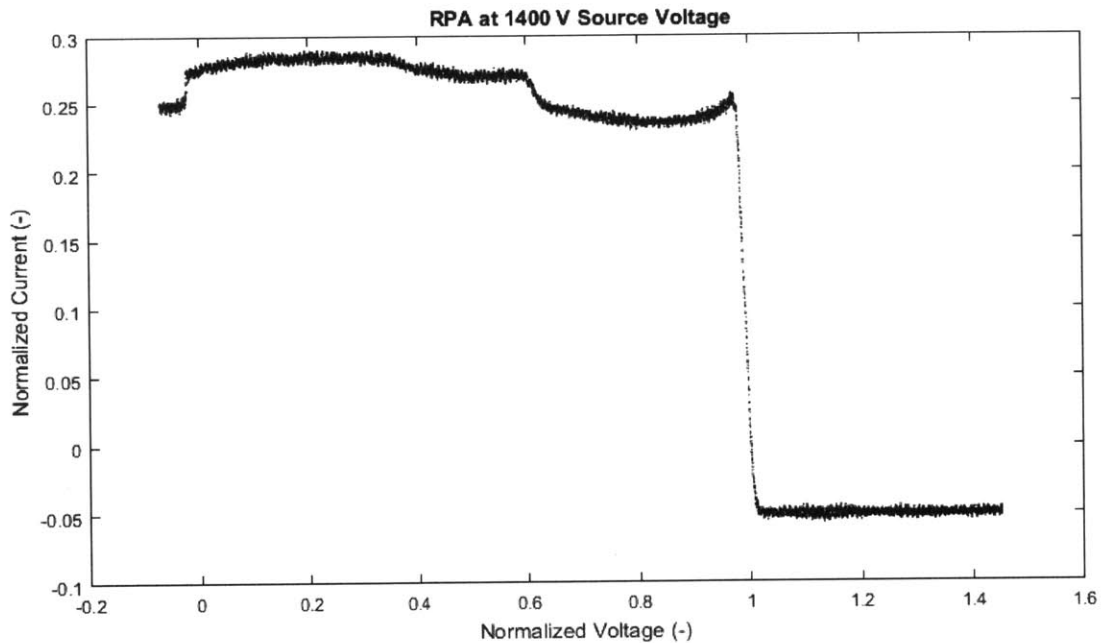

Figure 5-4 – RPA scan at 1400 V Source Voltage

Measuring the full width at half maximum (FWHM) of the signal around the value of 1 of normalized voltage reveals the most likely energy of monoenergetic ions and how narrow or wide the energy spread is. The data processing involves fitting the data to a smooth curve (a spline in this case), taking the derivative of the current with respect to the voltage and plotting the negative of the derivative as a function of voltage. The averaged true source voltage is 1418.757 V. The plot in Figure 5-5 shows a maximum at 0.9909 normalized voltage which translates into 1406 V. The FWHM is 0.0256 or 36 V.

72

Figure 5-6 shows a RPA scan for the negative mode at -1700 V. There are two steps at ~0.28 and 0.6 normalized voltages which are consistent with theoretical results. The fragmentation of dimers into monomers in the negative mode has the value of 0.305 (= 87 / (87 x 2 + 111)) and the fragmentation of trimers into dimers has the value of 0.59 (= (87 x 2 + 111) / (87 x 3 + 111 x 2)). The averaged emitted current is -108.4 nA.

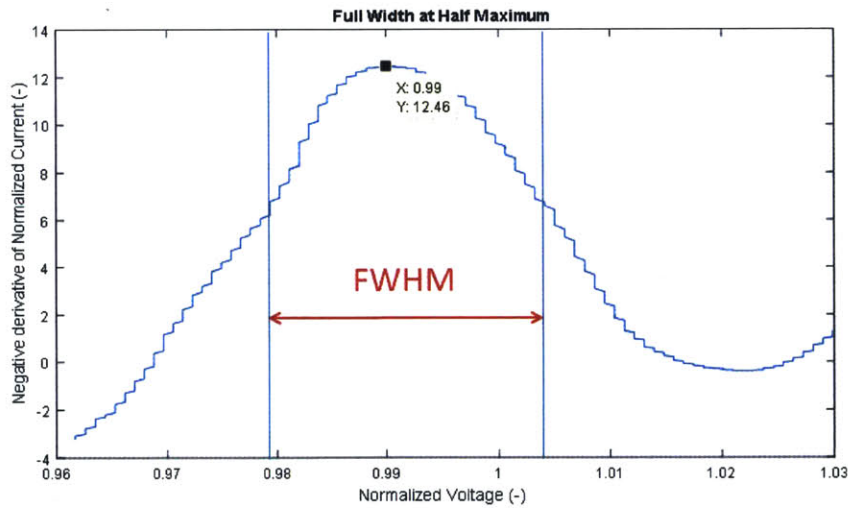Several RPA scans are presented in Appendix A.

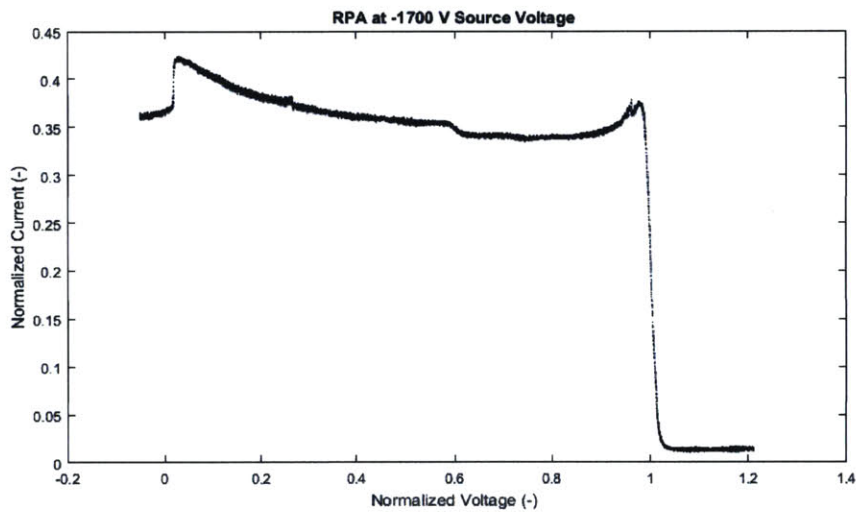Figure 5-5 – Full Width at Half Maximum at 1400 V Source Voltage

Figure 5-6 – RPA scan at -1700 V Source Voltage

73

5.3 Time of Flight Mass Spectrometry

The gate of the time of flight detector is pulsed at +/- 950 V at a 500 Hz frequency. The Channeltron voltage is set to -2.5 kV. The fragmented species have lower energies than the monoenergetic population and their deflection angle differ. Time of flight measurements are taken for the positive mode only and the emitted current is not stable. This may be caused by multiple emission sites turning on and off or by the ion beam moving around. Figure 5-7 shows a TOF scan for 1670 V source voltage.

The first step represents the monomers, the second step the dimers and the third steps the trimers. The signal to noise ratio allows for distinguishing main features but might be relatively low at the long times. There are no droplet signals within the noise level. Therefore, it can be concluded that the pure ionic regime (PIR) is achieved. The droplets are heavier and therefore slower and would appear at hundreds of microseconds of flight time.

The first step occurs between ~11 microseconds and ~20 microseconds. Dividing the monomer to dimer flight times (11/20 = 0.55) should equal the ratio of masses ($\sqrt{m_{mon}/m_{di}} = \sqrt{111/(111*2+87)} = 0.59$). The second step occurs between ~20 microseconds and ~27 microseconds. The monomer to trimer ratio (11/27 = 0.4) has a value close to the mass ratio of monomers to trimers ($\sqrt{m_{mon}/m_{di}} = \sqrt{111/(111*3+87*2)} = 0.46$). These calculations confirm that flight time steps are representative of the EMI-BF$_4$ ionic liquid.
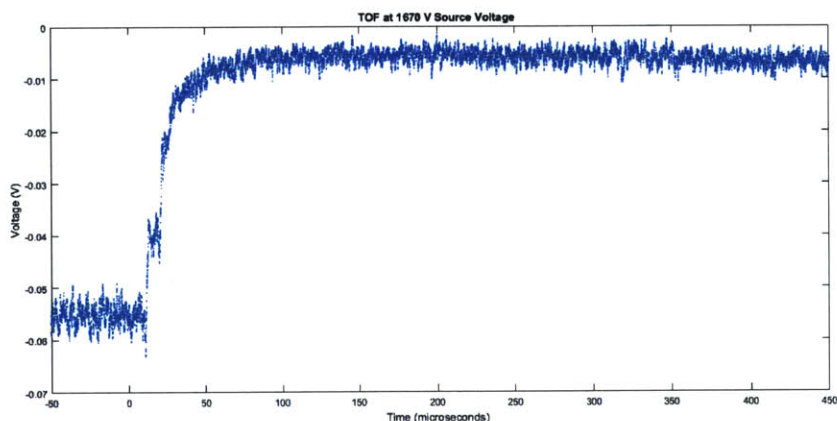

Figure 5-7 – TOF scan at 1670 V Source Voltage

By looking at the height of the steps we can measure the percentage of ions that are monomers, dimers and trimers. The height of the first step is 0.015 (from -0.04 V to -0.055 V). The final step occurs at -0.008 V. The total height is 0.047 (-0.008 + 0.055). The ratio of the first step height to the total height gives the percentage of the ions that are monomers for this measurement. The ratio is 0.015/0.047 which results in 31 % monomer population. The height of the second step is 0.017 (from -0.023 V to -0.04 V). The ratio of the second step height to the total height gives the percentage of ions that are dimers. The percentage of dimers is 36 %. The percentage of trimers is 19 %.

A second TOF scan is shown in Figure 5-8 for 1700 V source voltage. Measurements on the graph reveal a 36 % monomer population and a 38 % dimer population. Several TOF scans are presented in Appendix B.
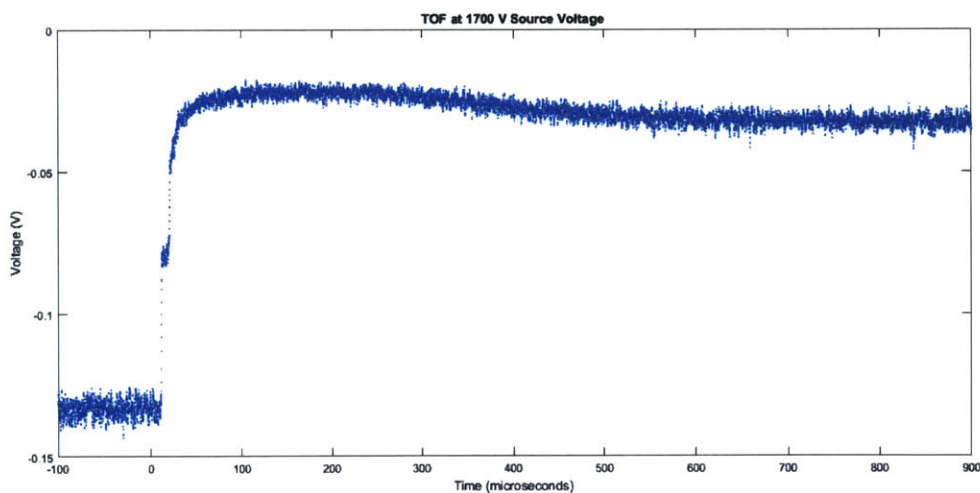

Figure 5-8 – TOF scan for 1700 V Source Voltage

5.4 Pure ionic regime (PIR)

When the ionic liquid is electrostatically stressed so that surface tension balances electrostatic traction a Taylor cone forms. The normal electric field at the apex is amplified and when it reaches a critical value E^* charges are removed. This value represents the field required to

75

produce evaporation of ions from the ionic liquid. If the hydraulic impedance in the emitter tip is high enough as to produce a small ratio of flow rate (Q) to electrical conductivity (K), the pure ionic regime can be obtained [22].

Using Darcy's law the pressure drop between the porous bulk of the emitter and the emission site can be estimated by

$$\vec{q}_s = -\frac{k}{\mu} \nabla P$$

where $\vec{q}_s$ is the volume flow rate per surface area (m/s), k is the material permeability, μ is the fluid viscosity and ∇P is the pressure gradient. For a conical geometry the pressure drop schematics is show in Figure 5-9. The pressure drop is calculated as the difference between the internal pressure near the emission site $(P(r_0))$ and the pressure in the bulk (P_C). The flow distribution is estimated by assuming radial flow through a spherical cap [3]. The pressure drop is given by

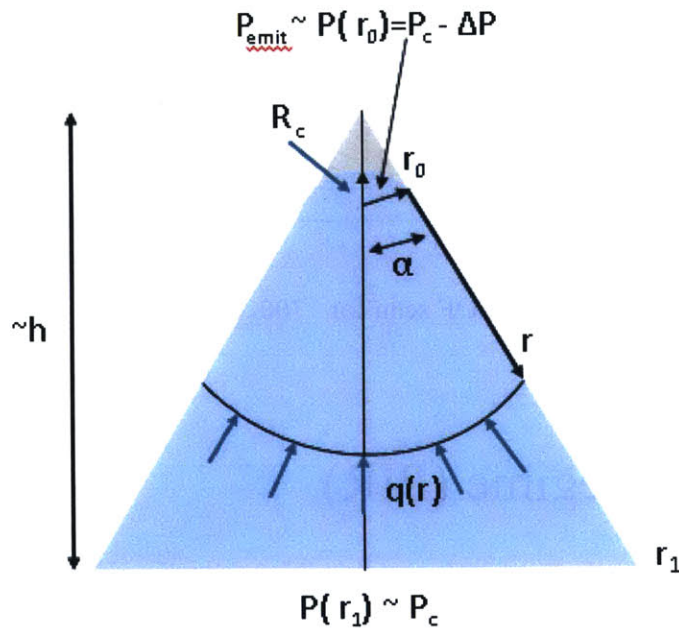$$\Delta P = -\frac{\mu}{k} \int_{r_0}^{r_1} \frac{-Q}{2 \pi r^2 (1 - \cos \alpha)} \, dr$$

Figure 5-9 – Conical geometry used to estimate the pressure drop between the base of the emitter and near the emission site [3]

76

The hydraulic impedance $Z = \Delta P / Q$ of a porous conical structure can be calculated as a function of viscosity of ionic liquid (0.038 Pa for EMI-BF$_4$), substrate permeability (k), half angle (α), radius of curvature (R_c) and height (h) [3] and is given by

$$Z = \frac{\mu}{2\pi k} \frac{1}{1 - \cos \alpha} \left(\frac{\tan \alpha}{R_c} - \frac{\cos \alpha}{h} \right)$$

The lowest impedance for which PIR was achieved with EMI-BF$_4$ is 1.5 x 10^{17} kg s^{-1} m^{-4} [22, 40]. The impedance in the equation above is governed by the first term only for high aspect ratio emitters (h/R$_c$ > 10).

The substrate permeability can be calculated with the formula

$$k = r_p^2 \left(60 \left(1 - \emptyset_p \right)^2 \right)^{-1}$$

where r_p is the pore size and $\emptyset_p$ is the porosity [22, 3].

By plugging in the value of impedance for which PIR is achieved and the characteristic values for the tungsten needle from which the carbon xerogel emitter tip is molded: half angle (α) = 20° and radius of curvature (R_c) = 10 μm we obtain a permeability k = 1.5 x 10^{-14} m^2. A value of porosity $\emptyset_p$ = 0.6 [19] results in a pore size diameter requirement of ~0.8 μm for PIR. The pressure burst tests do not reveal the emergence of bubbles from the emitter tips. However, the pure ionic regime is demonstrated with time of flight mass spectrometry. It can be argued that the tip is porous having pore sizes smaller than 0.4 μm. This value results from equating the pressure at which bubbles emerge from the substrate to the Young-Laplace pressure at 33 psi. This is the highest pressure achievable with the laboratory equipment. It should be noted that the carbon substrates that were ground to the desired shape (therefore removing the skin) prior to molding the single tip burst at pressures as low as 1 psi. After the single emitters were molded, the substrates developed a second skin on their surface, which caused the bubbles not to emerge or to emerge at higher pressures from the substrate. Moreover, once there is flow the pressure does not remain uniform, but drops in the material, and therefore we do not know if the pressure "inside" the tip was 33 psi or lower. The SEM images of the tip are not conclusive on the existence and size of pores.

Several possibilities of transporting ionic liquid to the emission site can be envisaged. Figure 5-10 shows two possibilities of liquid transport. In the first case both the substrate and the tip are porous. In the second case only the substrate is porous and the emitter is externally wetted. The emitter could be also formed exclusively of skin and be hollow. A hybrid of the two is also possible.
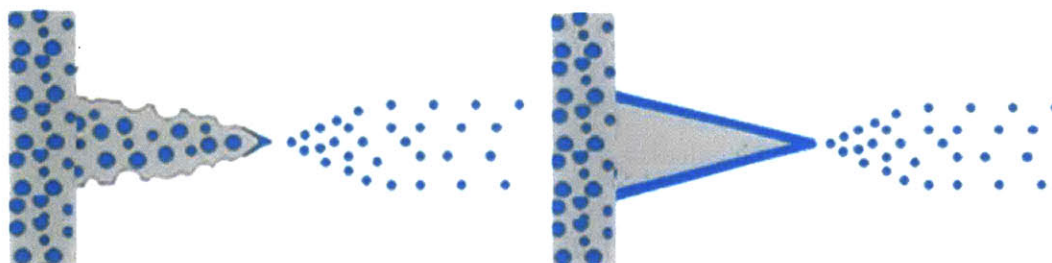

Figure 5-10 – Possibilities of liquid transport: a) internally wetted emitter; b) externally wetted emitter

Chapter 6

Conclusions

Carbon xerogel substrates were synthesized for applications in space propulsion. Carbon xerogels were selected due to their exceptional properties such as large surface to volume ratio, robustness, ability to transport ionic liquid and pore size uniformity. A synthesis route is much more advantageous for reproducibility. The selected fabrication technique was molding of emitter tips as this allows for batch manufacturing and repeatability.

The synthesis route mixes resorcinol and formaldehyde in the presence of acetic acid. The solution was poured into molds and allowed to gel, cure and dry for specific amounts of time. The resulting resorcinol formaldehyde xerogels were then pyrolyzed in an inert atmosphere to create the carbon xerogels. The xerogels exhibited shrinkage during the curing and pyrolysis steps. The substrates were subsequently ground and polished to the desired dimensions. The material used for creating the molds was PDMS, a non-toxic and biocompatible material used in microfluidic applications, which conveys a very high fidelity of the mold.

Carbon xerogel tips were molded on previously synthesized carbon xerogel substrates. Retarding potential analysis and Time of Flight Mass Spectrometry experiments were performed to probe the fragmentation fractions and beam composition. The results of the RPA were consistent with fragmentation fractions of the EMI-BF$_4$ ionic liquid. The beam was nearly monoenergetic and fragmentation occurred mostly outside the acceleration region. Acceleration outside the acceleration region does not affect the thruster efficiency. Emission for the TOF experiment was not stable and this was likely caused by the ion beam moving around or by multiple emission sites turning on and off. The percentages of monomer, dimer and trimer populations were calculated for several TOF scans from measurements on the plots. The results were consistent with the pure ionic regime. The transport of ionic liquid was most likely performed internally through the porous bulk of the substrate and either internally or externally on the emitter tip.

Carbon xerogel arrays were molded on top of previously synthesized carbon xerogel substrates. The molds were obtained from laser ablated porous borosilicate glass arrays that were

coated with Teflon. The material used for the molds was PDMS. Testing of the carbon arrays was not performed and future work should include testing the arrays. This requires perfect alignment of an extractor electrode. It should be noted that the molded arrays were not integrated on frames, which would allow for alignment.

The carbon xerogels substrates exhibited shrinkage, deflection and the formation of a skin with different pore sizes than the bulk. Deflection was not observed in the molded carbon tips as these cured inside PDMS molds. Deflection could be associated to samples being in contact with the atmosphere. For molding arrays it could be argued that the tips shrink compared to the mold. However, if the tips shrink with respect to their axis of symmetry, there should be no alignment issues. Shearing at the contact of the emitter substrate and the molded tips caused by different shrinkage rates (the substrate undergoes pyrolysis twice) should also be investigated.

The ultimate goal of molding carbon xerogel emitter arrays is to allow for increasing the thrust density of ion electrospray thrusters. This could be achieved by decreasing the distance between adjacent tips for the same surface area of the emitter substrate. Due to their exceptional properties, carbon xerogels are suited candidates for molding such arrays. The limitations on the spacing between tips are given by space charge, electrochemistry and hydraulics and the smallest achievable spacing is estimated at ~1-10 μm (compared to 450 μm for the state of the art emitter arrays) [1].

Appendix A

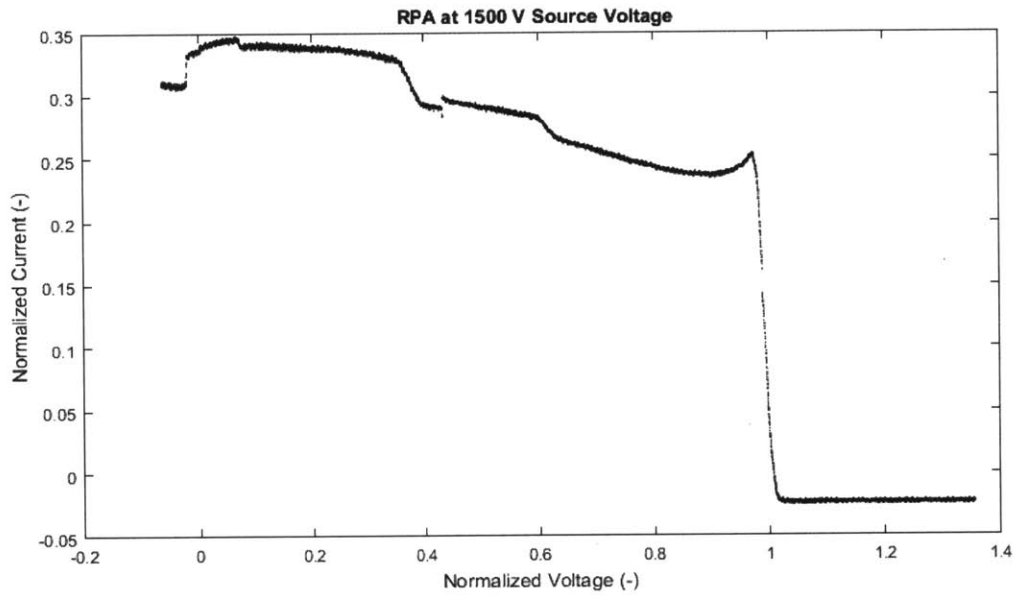Supplementary Retarding Potential Analysis Data

Figure A-1 – RPA scan at 1500 V Source Voltage (146 nA averaged emitted current)
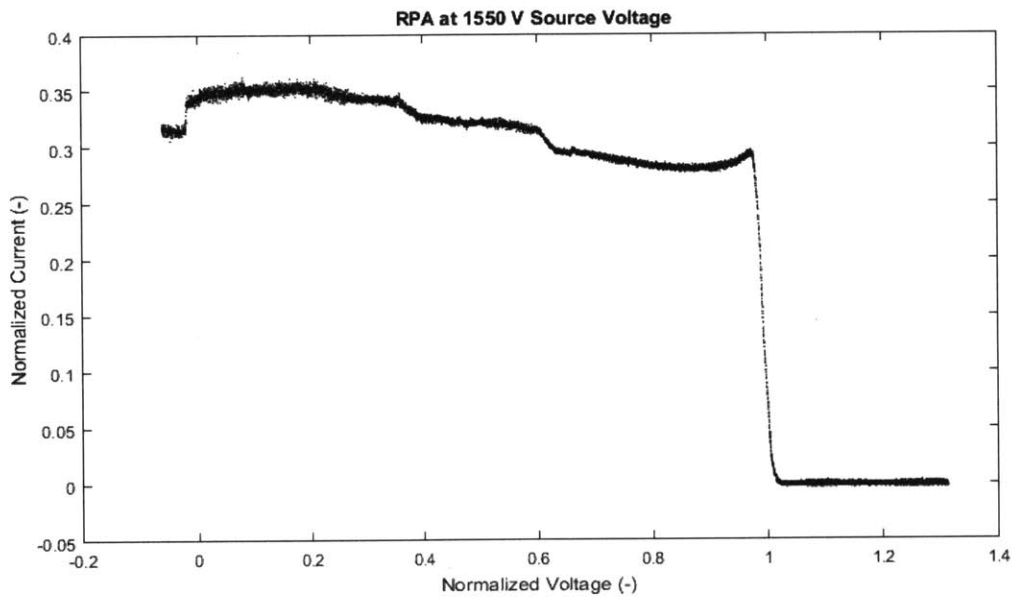

Figure A-2 – RPA scan at 1550 V Source Voltage (196 nA averaged emitted current)
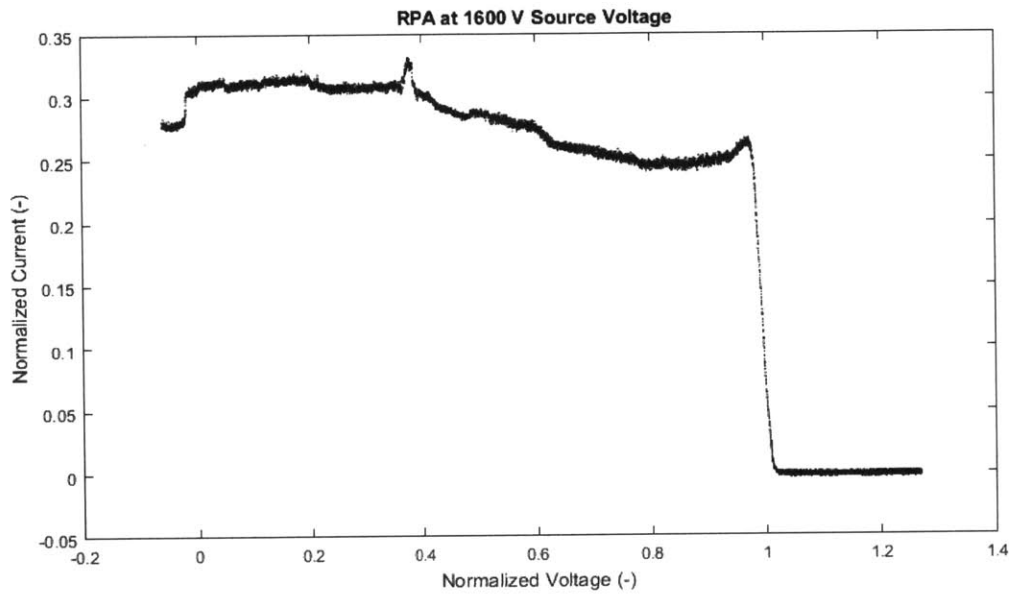
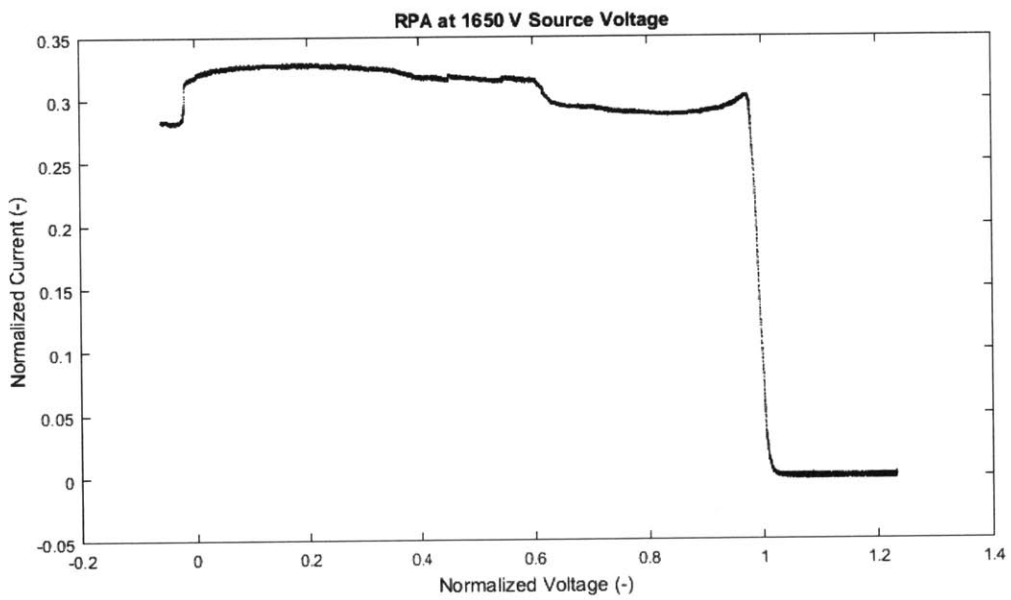Figure A-3 – RPA scan at 1600 V Source Voltage (223 nA averaged emitted current)

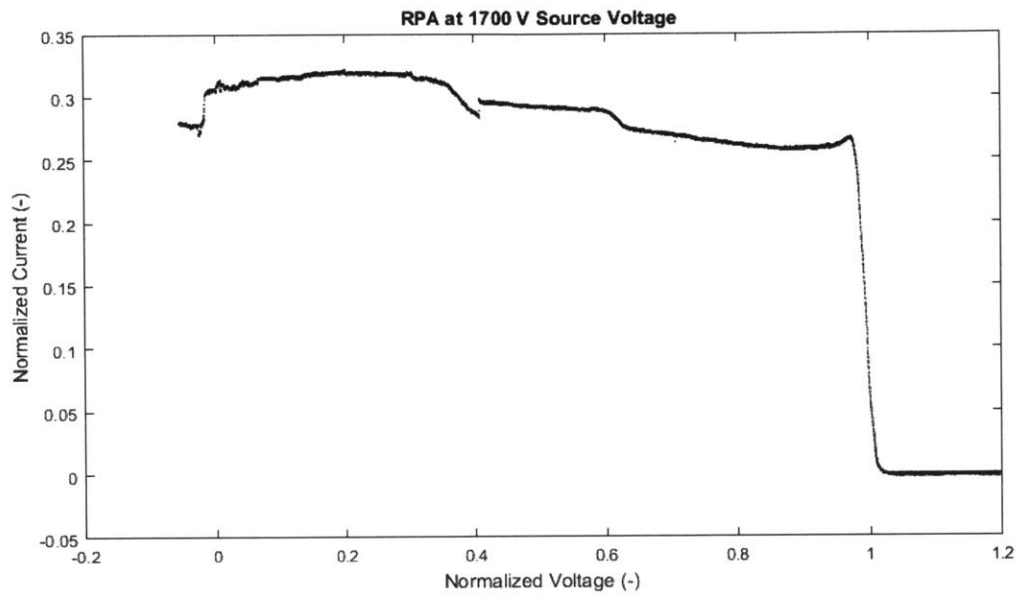Figure A-4 – RPA scan at 1650 V Source Voltage (269 nA averaged emitted current)

Figure A-5 – RPA scan at 1700 V Source Voltage (317 nA averaged emitted current)
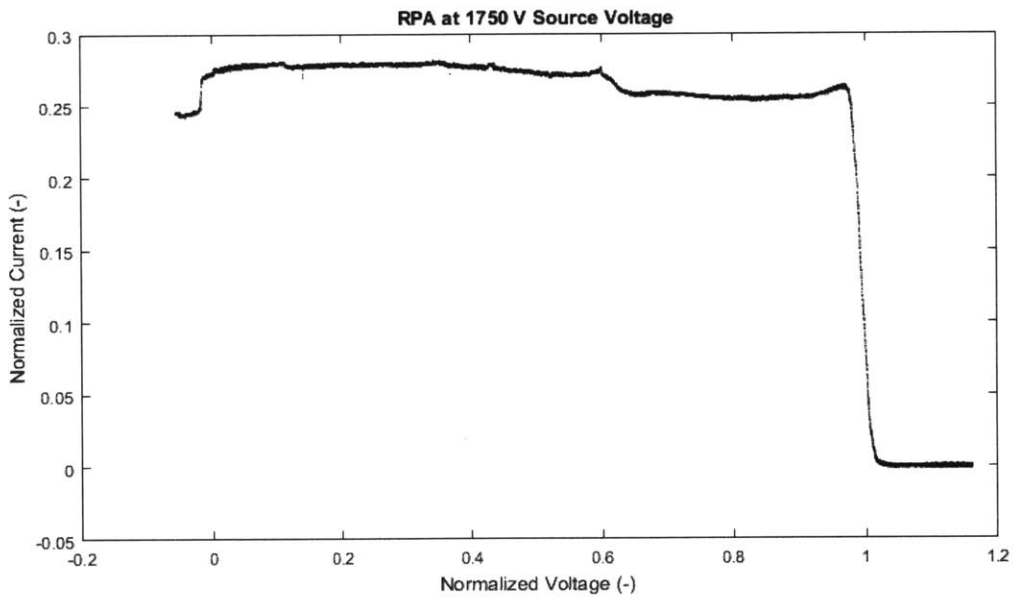

Figure A-6 – RPA scan at 1750 V Source Voltage (295 nA averaged emitted current)
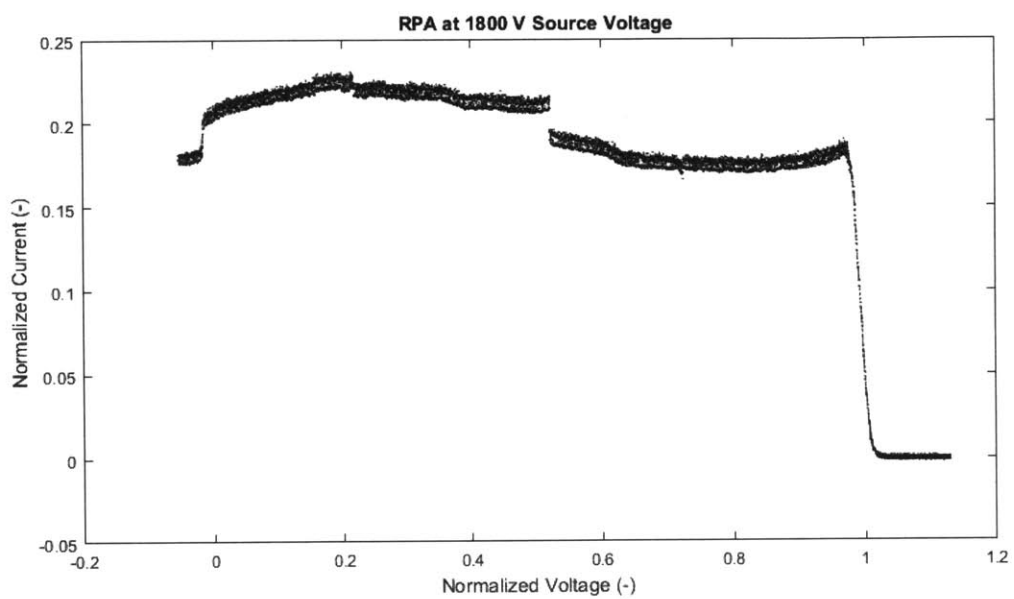
Figure A-7 – RPA scan at 1800 V Source Voltage (325 nA averaged emitted current)
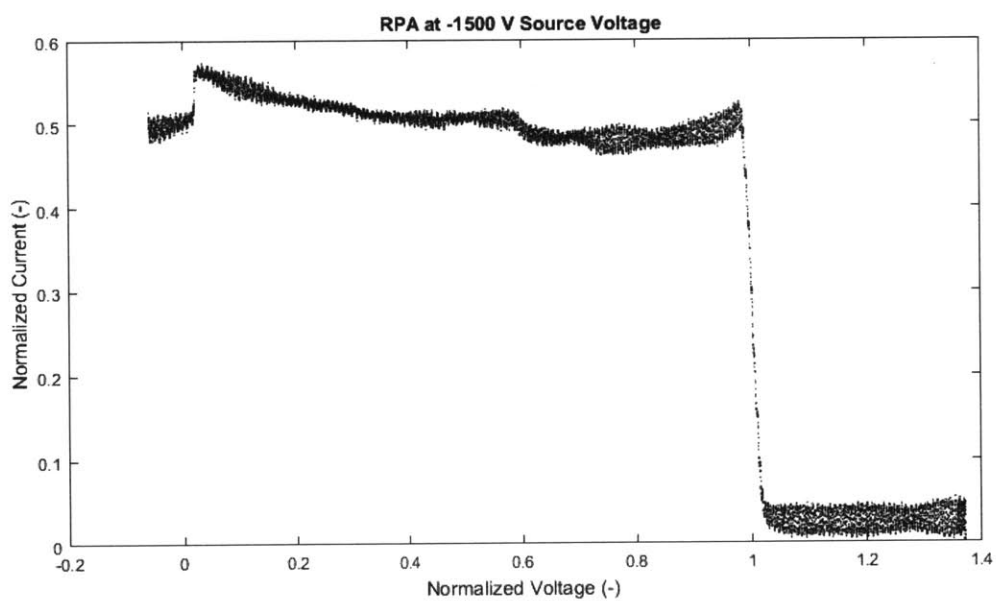

Figure A-8 – RPA scan at -1500 V Source Voltage (-38 nA averaged emitted current)
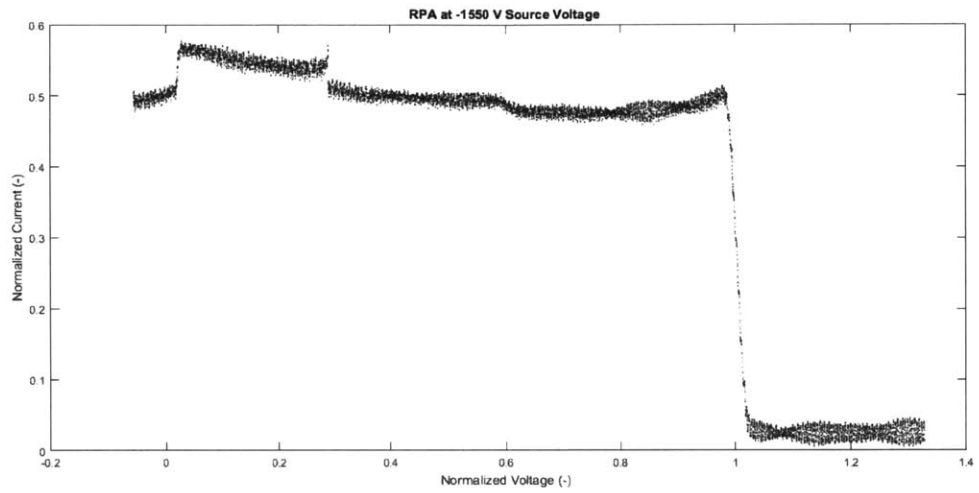
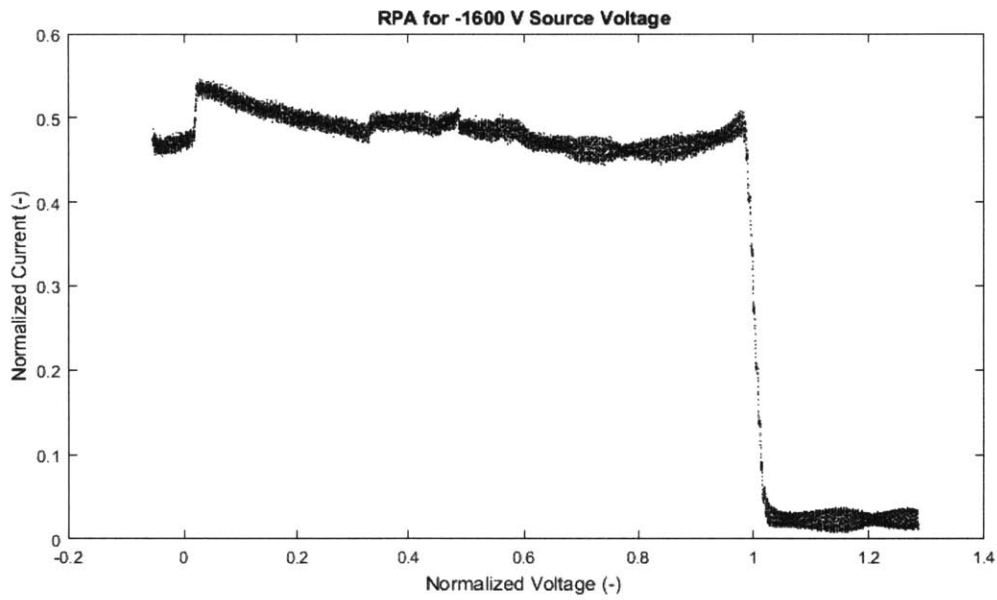Figure A-9 – RPA scan at -1550 V Source Voltage (-43 nA averaged emitted current)

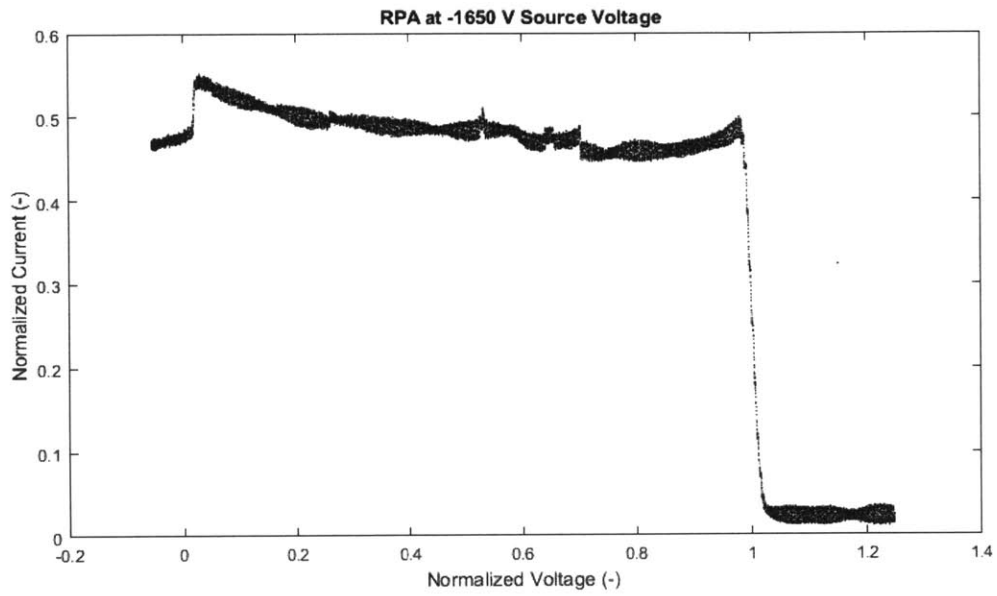Figure A-10 – RPA scan at -1600 V Source Voltage (-55 nA averaged emitted current)

Figure A-11 – RPA scan at -1650 V Source Voltage (-66 nA averaged emitted current)
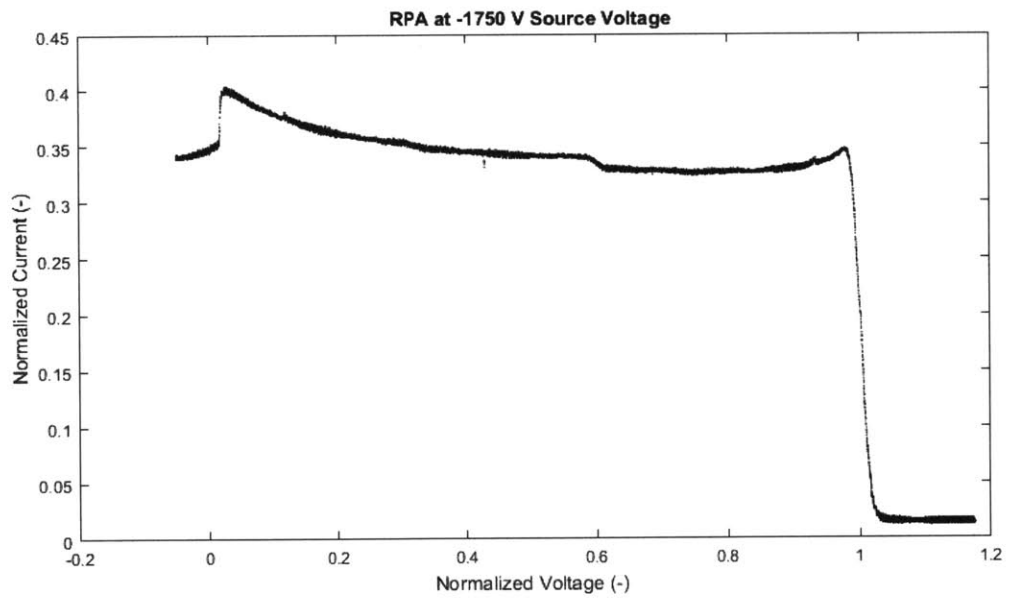

Figure A-12 – RPA scan at -1750 V Source Voltage (-150 nA averaged emitted current)
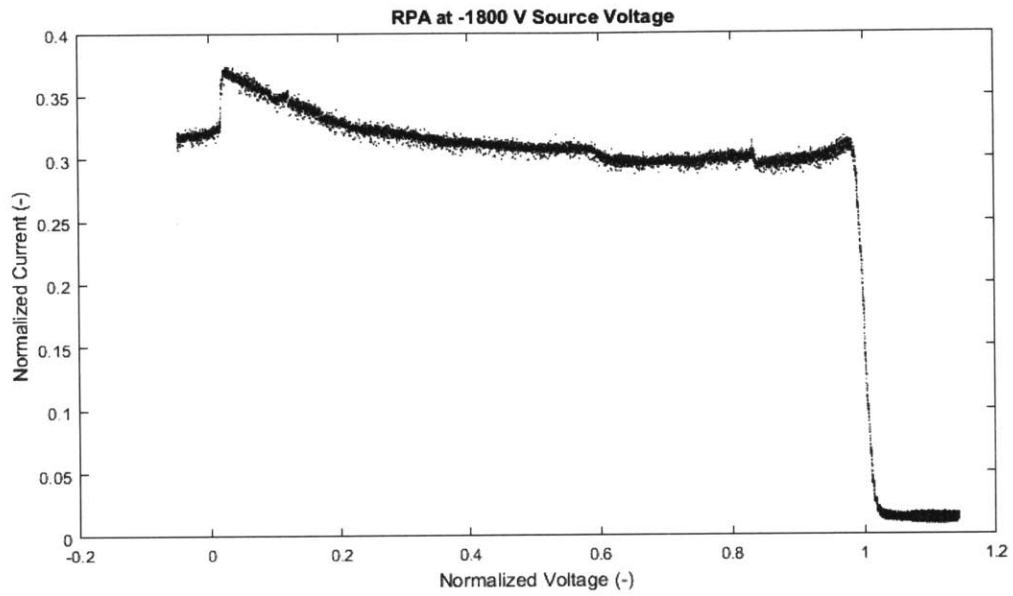
Figure A-13 – RPA scan at -1800 V Source Voltage (-152 nA averaged emitted current)

Appendix B

Supplementary Time of Flight Mass Spectrometry Data
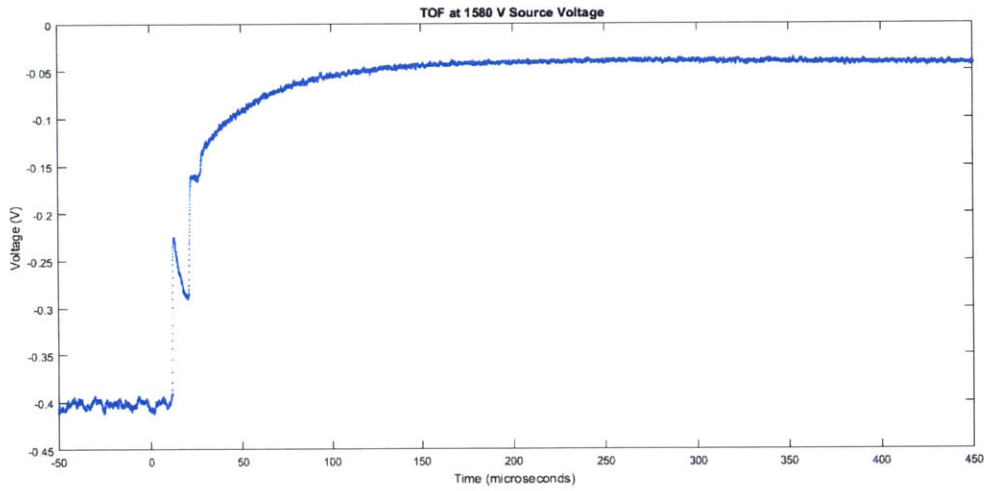

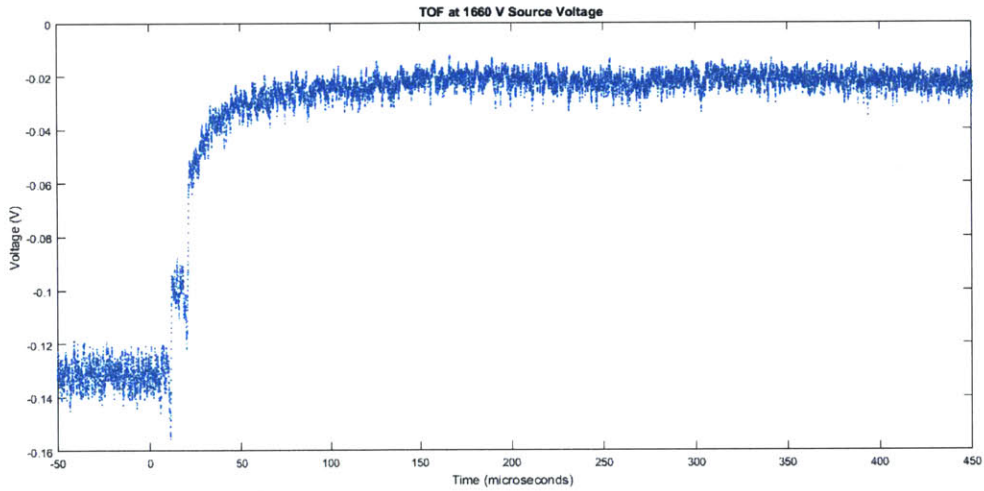Figure B-1 – TOF at 1500 V Source Voltage
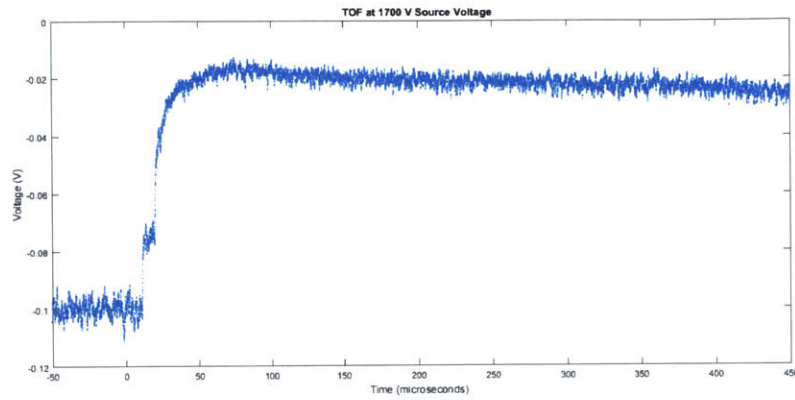

Figure B-2 – TOF at 1660 V Source Voltage

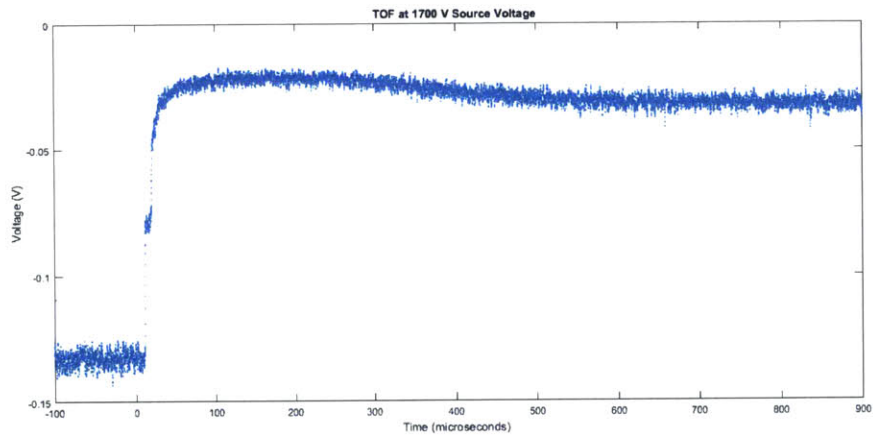Figure B-3 – TOF at 1700 V Source Voltage
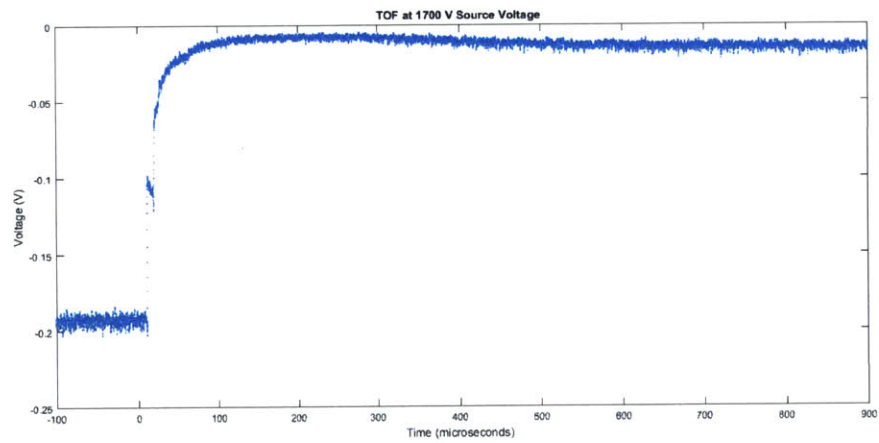

Figure B-4 – TOF at 1700 V Source Voltage

Figure B-5 – TOF at 1700 V Source Voltage

References

1. Lozano, P., C. (2015). *Spacecraft propulsion class notes*, Massachusetts Institute of Technology, Cambridge, MA.

2. Coffman, C., Perna, L., Li, H. and Lozano, P., C. (2013). On the manufacturing and emission characteristics of a novel borosilicate electrospray source, *49th AIAA/ASME/SAE ASEE Joint Propulsion Conference*, July 14-17, San Jose, CA.

3. Courtney, D., G. (2011). *Ionic Liquid Ion Source Emitter Arrays Fabricated on Bulk Porous Substrates for Spacecraft Propulsion*, Ph.D. thesis, June, Massachusetts Institute of Technology, Cambridge, MA.

4. Guerra-Garcia, C., Krejci, D. and Lozano, P. (2016). Spatial uniformity of the current emitted by an array of passively fed electrospray porous emitters, *Journal of Physics D: Applied Physics*, 49(11)

5. Krpoun, R. and Shea, H., R. (2009). Integrated out-of-plane nanoelectrospray thruster arrays for spacecraft propulsion, *Journal of Micromechanics and Microengineering*, 19(4):045019.

6. Garza, T., C. (2007). *Optimizing Wettability of Externally Wetted Microfabricated Silicon Electrospay Thrusters*, M.S. Thesis, June, Massachusetts Institute of Technology, Cambridge, MA.

7. Velasquez-Garcia, L., F. (2001). *A Microfabricated Colloid Thruster Array*, M.S. Thesis, June, Massachusetts Institute of Technology, Cambridge, MA.

8. Velasquez-Garcia, L., F. (2004). *The Design, Fabrication and Testing of Micro-fabricated Linear and Planar Colloid Thruster Arrays*, Ph.D. Thesis, June, Massachusetts Institute of Technology, Cambridge, MA.

9. Gassend, B. (2007). *A Fully Microfabricated Two-Dimensional Electrospray Array with Applications to Space Propulsion*, Ph.D. Thesis, Massachusetts Institute of Technology, Cambridge, MA.

10. Gassend, B., Velasquez-Garcia, L., F., Akinwande, A., I., and Martinez-Sanchez, M. (2009). A microfabricated planar electrospray array ionic liquid ion source with integrated extractor, *Journal of Micromechanical Systems*, 18(3):679-694.

11. Legge, R., S., Lozano, P., C. and Martinez-Sanchez, M. (2007). Fabrication and characterization of porous metal emitters for electrospray thrusters. *30th International Electric Propulsion Conference,* September 17-20, Florence, Italy.

12. Legge, S., R., Jr. (2008) *Fabrication and characterization of porous metal emitters for electrospray propulsion applications,* M.S. thesis, June, Massachusetts Institute of Technology, Cambridge, MA.

13. Legge, R., S. and Lozano, P., C. (2011). Electrospray Propulsion Based on Emitters Microfabricated in Porous Metals, *Journal of Propulsion and Power,* 27 (2), 485-495.

14. Lozano, P., C. and Martinez-Sanchez, M. (2005). Ionic liquid ion sources: Characterization of externally wetted emitters. *Journal of Colloid and Interface Science,* 282(2):415-421.

15. Lozano, P., C. And Martinez-Sanchez, M (2004). Ionic liquid ion sources: suppression of electrochemical reactions using voltage alternation. *Journal of Colloid and Interface Science,* 280(1):149-154, 2004.

16. Brikner, N. and Lozano, P., C. (2012) The role of upstream distal electrodes in mitigating electrochemical degradation of ionic liquid ion sources. *Applied Physics Letters,* 101.

17. Brikner, N. and Lozano, P., C. (2013). Physical Limitations on the Lifetime of Ionic Liquid Ion Sources, *49th AIAA/ASME/SAE ASEE Joint Propulsion Conference,* July 14-17, San Jose, CA.

18. Xie, J. (2014). *Fabrication and Characterization of Sintered Porous Glass Emitters for Electrospray Propulsion,* M.S. thesis, June, Massachusetts Institute of Technology, Cambridge, MA.

19. Arestie, S. (2014). *Porous Material and Process Development for Electrospray Propulsion Applications.* M.S. thesis, June, Massachusetts Institute of Technology, Cambridge, MA.

20. Tokudome, Y., Fujita, K. and Nakanishi, K. (2007). Synthesis of monolithic Al_2O_3 with well-defined macropores and mesostructured skeletons via the sol-gel process accompanied by phase separation. *Chemistry of Materials,* 19:3393-3398.

21. Krejci, D., Mier-Hicks, F., Fucetola, C., and Lozano, P., C. (2015). Design and characterization of a scalable ion electrospray propulsion system, *30th International*

Symposium on Space Technology and Science, 34th International Electric Propulsion Conference, 6th Nano-satellite Symposium, July 4-10, Hyogo-Kobe, Japan.

22. Perez-Martinez, C., S. and Lozano, P., C. (2015). Ion field-evaporation from ionic liquids infusing carbon xerogel microtips, *Applied Physics Letters*, 107.

23. Mulik, S. and Sotiriou-Leventis, C. (2011). Resorcinol Formaldehyde Aerogels. M. A. Aegerter et al. (eds.), *Aerogels Handbook, Advances in Sol-Gel Derived Materials and Technologies*, Springer Science+Business Media.

24. Pekala, R., W. (1989). Organic aerogels from the polycondensation of resorcinol with formaldehyde, *Journal of Materials Science*, 24:3221-3227.

25. Pierre, A. and Pajonk, G. (2002) Chemistry of Aerogels and Their Applications, *Chemical Reviews*, 102: 4243-4265.

26. Baumann, T, F., Worsley, M., A., Han, T., Y. – J. and Satcher Jr, J., H. (2008). High surface area carbon aerogel monoliths with hierarchical porosity, *Journal of Non-Crystalline Solids,* 354: 3513-3515.

27. Al-Muhtaseb, S., A. and Ritter, J., A. (2003). Preparation and Properties of Resorcinol-Formaldehyde Organic and Carbon Gels. *Advanced Materials*, 15: 101-114.

28. Brandt, R., Petricevic, R., Probstle, H. and Fricke, J. (2003) Acetic acid catalyzed carbon aerogels, *Journal of Porous Materials*, 10:171-178, (9).

29. Yao, M., Fang, J. (2012). Hydrophilic PEO-PDMS for microfluidic applications, *Journal of Micromechanics and Microengineering*, 22 025012 (6pp) (10).

30. Meniscus, https://en.wikipedia.org/wiki/Meniscus, accessed April 18, 2016.

31. Rojas-Herrera, J. (2016), personal correspondence, Massachusetts Institute of Technology, Cambridge, MA.

32. Perez-Martinez, C. (2016), personal correspondence, Massachusetts Institute of Technology, Cambridge, MA.

33. Miller, C., E. (2016), personal correspondence, Massachusetts Institute of Technology, Cambridge, MA.

34. Dahiya, R., S. and Lorenzelli, L. (2012) Removing Cured PDMS from Micro/Nano-structures, *Microelectronic Engineering.*

35. Petricevic, R., Glora, M., Fricke, J. (2000). Planar fibre reinforced carbon aerogels for application in PEM fuel cells, *Carbon*, 39:857-867.

36. Miller, C., E. (2015). *On the Stability of Complex Ions in Ionic Liquid Ion Sources*, M.S. thesis, June, Massachusetts Institute of Technology, Cambridge, MA.

37. Lozano, P. (2006). Energy properties of an EMI-Im ionic liquid ion source, *Journal Of Physics D-Applied Physics*, 39 (1), 126-134.

38. Miller, C. (2015). The effects of metastable solvated ions on electrospray ion thruster efficiency, *30th International Symposium on Space Technology and Science, 34th International Electric Propulsion Conference, 6th Nano-satellite Symposium*, July 4-10, Hyogo-Kobe, Japan.

39. Jivanescu, I., E., Rojas-Herrera, J., Freeman, D., Krejci, D., Fucetola, C. and Lozano, P., C. (2015). Porous materials for ion-electrospray spacecraft micro-engines, *Journal of Nanomechanics and Micromechanics*, under review

40. Krpoun, R., Smith, K., L, Stark, J., P., W. and Shea, H. R. (2009). Tailoring the hydraulic impedance of out-of-plane micromachined electrospray sources with integrated electrodes, *Applied Physics Letters*, 94, 163502.